Perpendicular magnetic anisotropy in amorphous Nd_xCo_{1-x} thin films studied by x-ray magnetic circular dichroism

R. Cid,[1,*] J. M. Alameda,[1,2] S. M. Valvidares,[3,†] J. C. Cezar,[3,‡] P. Bencok,[3,‖] N. B. Brookes,[3] and J. Díaz[1,2,§]

[1]*Universidad de Oviedo, Avenida de Calvo Sotelo s/n, Oviedo 33007, Spain*

[2]*CINN (CSIC-Universidad de Oviedo-Principado de Asturias), 33940 El Entrego, Spain*

[3]*European Synchrotron Radiation Facility, CS40220, F-38043 Grenoble Cedex, France*

(Received 28 October 2016; revised manuscript received 9 May 2017; published 1 June 2017)

The origin of perpendicular magnetic anisotropy (PMA) in amorphous Nd_xCo_{1-x} thin films is investigated using x-ray magnetic circular dichroism (XMCD) spectroscopy at the Co $L_{2,3}$ and Nd $M_{4,5}$ edges. The magnetic orbital and spin moments of the $3d$ cobalt and $4f$ neodymium electrons were measured as a function of the magnetic field orientation, neodymium concentration, and temperature. In all the studied samples, the magnetic anisotropy of the neodymium subnetwork is always oriented perpendicular to the plane, whereas the anisotropy of the orbital moment of cobalt is in the basal plane. The ratio L_z/S_z of the neodymium $4f$ orbitals changes with the sample orientation angle, being higher and closer to the atomic expected value at normal orientation and smaller at grazing angles. This result is well explained by assuming that the $4f$ orbital is distorted by the effect of an anisotropic crystal field when it is magnetized along its hard axis, clearly indicating that the $4f$ states are not rotationally invariant. The magnetic anisotropy energy associated to the neodymium subnetwork should be proportional to this distortion, which we demonstrate is accessible by applying the XMCD sum rules for the spin and intensity at the Nd $M_{4,5}$ edges. The analysis unveils a significant portion of neodymium atoms magnetically uncoupled to cobalt, i.e., paramagnetic, confirming the inhomogeneity of the films and the presence of a highly disordered neodymium rich phase already detected by extended x-ray-absorption fine structure (EXAFS) spectroscopy. The presence of these inhomogeneities is inherent to the evaporation preparation method when the chosen concentration in the alloy is far from its eutectic concentrations. An interesting consequence of the particular way in which cobalt and neodymium segregates in this system is the enhancement of the cobalt spin moment which reaches 1.95 μ_B in the sample with the largest segregation.

DOI: 10.1103/PhysRevB.95.224402

I. INTRODUCTION

The perpendicular magnetic anisotropy (PMA) in amorphous rare-earth–transition metal (RE-TM) alloys has been the subject of intense study since PMA was observed in GdCo amorphous alloys, decades ago [1]. Nowadays, these types of materials still attract great attention since they are used as base materials for the study of novel micro and nanoscopic magnetic phenomena [2–4]. The amorphous structure of the magnetic material used in some of these investigations [5–7] allows a larger miniaturization, faster preparation process, and more freedom in the choice of the relevant parameters than polycrystalline or monocrystalline materials, especially in the tune of its PMA energy.

Most of the studies agree in attributing the origin of the PMA in these alloys to the rear-earth (RE) subnetwork due to a local anisotropic crystal field caused by distortions at its local environment [8–10]. The perturbations of the RE environment are experimentally reported as being produced by structural anisotropies in bonding [11] and/or coordination [12] generated during the deposition process [13,14]. In all these experiments, the structural anisotropy is proved at an atomic level but its correlation with the magnetic anisotropy is always done in an indirect way. None of those experiments demonstrates how the structural changes affect the magnetism of the TM and RE subnetworks separately. For instance, it has never been determined if the magnetic anisotropy of the TM subnetwork improves or reduces the PMA of the alloy.

It is well known that the highest PMA energy in these alloys happens at a specific small range of RE concentrations, between 20% and 25% atomic neodymium concentration in the case of NdCo alloys [15]. However, the reason why this occurs is totally unclear. It has been hypothesized that the atomic arrangement around neodymium at short distances is similar to the relaxed crystalline arrangement for that specific concentration ($NdCo_5$ crystal [16]). A previous structural study of our NdCo amorphous alloys by extended x-ray-absorption fine structure (EXAFS) spectroscopy with samples whose PMA energy doubled that reported previously demonstrated that this is not the case. The atomic arrangement of neodymium in these samples is so disordered that it can not be detected by EXAFS [17]. Only the cobalt subnetwork detected by EXAFS is anisotropic in coordination and bond length [17] in agreement with what has been observed in other RE-TM systems [11,12].

The aim of the experiment presented in this work is to understand the conditions that give rise to PMA in these alloys by observing the changes in the magnetic moment and the

*Present address: European Synchrotron Radiation Facility-SpLine (ICMM/CSIC), CS40220, F-38043 Grenoble Cedex, France.

†Present address: ALBA Synchrotron Light Source, Cerdanyola del Valles 08290, Spain.

‡Present address: Brazilian Synchrotron Light Laboratory (LNLS), National Center for Research in Energy and Materials (CNPEM), CP 6192, 13083-970, Campinas, SP, Brazil.

‖Present address: Diamond Light Source, Science Division, Didcot OX11 0DE, United Kingdom.

§jidiaz@uniovi.es

magnetic anisotropy in each of the magnetic subnetworks of the alloy at specific alloy concentrations and preparation conditions. XMCD spectroscopy is the technique of choice to investigate this at an atomic level [18]. It allows us to access the spin and orbital magnetic moments of the RE and the TM subnetworks separately [19–21]. Relatively few XMCD experiments have been made at the RE $M_{4,5}$ edges in order to study the $4f$ states, which carry the magnetic moment of the RE [4,22–27]. Moreover, to our knowledge, no experimental work has been done on the dependence of the $4f$ magnetic moment on the orientation of the magnetic field by XMCD [23,28], which is mandatory to understand PMA in RE-TM alloys. In this regard, the magnetocrystalline anisotropy of $3d$ metals is much more thoroughly studied by XMCD than RE [29–32].

The evidence for the magnetic anisotropy in the RE subnetwork should be given by the anisotropy in its magnetic moment [28]. Due to the atomic character of the $4f$ orbital, interatomic interactions like the crystal field and the indirect exchange are expected to have too little weight compared to the intratomic spin-orbit interaction and, therefore, no measurable changes are expected in the distribution of the $4f$ charge when it is reoriented with a magnetic field. This has been demonstrated to be not true in EuO crystals [28] and in amorphous $TbFe_2$ [33]. Actually, this present work proves that the $4f$ orbital of neodymium is not completely rotationally invariant in magnetically anisotropic amorphous NdCo alloys, demonstrating the contribution of the $4f$ states to the magnetic anisotropy energy. Moreover, here it is shown that it is possible to access the amount of distortion of the $4f$ charge by using the XMCD sum rules for the spin and the intensity. The comparison of the measurements between different samples with different anisotropies indicates that the amount of deformation in the $4f$ charge should be linked to the magnetic anisotropy energy of the RE subnetwork.

Although the magnetocrystalline anisotropy in $3d$ TM magnetic metals is usually associated with the anisotropy of the orbital moment (Δm_o) [34,35], the exact quantification of its energy needs to take into account other factors related to their atomic environment [30–32]. Our study will show that in NdCo alloys, this energy gets higher and it competes with that of the neodymium subnetwork when the cobalt magnetic moment gets more localized by bonding to neodymium, which it does without having to increase Δm_o but increases its orbital moment to spin ratio m_o/m_s.

The concentrations of the analyzed samples are chosen at the values where the PMA is known to be the highest, and at higher and lower cobalt concentrations. In this way, we intend to understand not only why the PMA energy is raised but also why it is extinguished. We must emphasize that the diversity of atomic environments accessible by changing the alloy concentration is restricted by the phase diagram of the alloy. This is an aspect that is rarely treated in amorphous thin films with the depth that it deserves [36]. The most amorphous liquidlike structure is produced only at the concentrations of the eutectic points [37] causing structural and concentration inhomogeneities in the alloys [38,39]. The singularly deep eutectic points in the light RE-Co alloys are located at the RE rich region, at 60%–80% atomic neodymium concentrations [40]. They are far from the concentrations where NdCo alloys show the highest PMA energy [15,41]. The presence of inhomogeneities in Nd_xCo_{1-x} ($0.16 < x < 0.22$) alloys has been previously evidenced by us using EXAFS [17] where it was shown that most of cobalt atoms were surrounded only by cobalt up to second neighbors at least, whereas no neighbors were detected in neodymium due to the strong disorder in its atomic environment. This proved the presence of two phases, one very rich in neodymium and amorphous, and a second phase made of very short-range ordered cobalt. One of the most remarkable consequences of this phase separation, observed in the present experiment, is the significant enhancement of the spin and orbital moment of cobalt in the cobalt rich alloys. This experiment also gives more proof of this phase separation by quantitatively evaluating its concentration.

TABLE I. Concentration and thickness of the samples analyzed in the experiment.

Sample	Composition	Nd concentration (%)	Thickness
NC10	$NdCo_{10.3}$	$9\% \pm 1\%$	265 Å
NC5	$NdCo_{3.9}$	$21\% \pm 1\%$	265 Å
MNC5	$NdCo_{3.5}$	$22\% \pm 1\%$	310 Å
NC2	$NdCo_{1.9}$	$34\% \pm 1\%$	310 Å
NC	$NdCo_{0.8}$	$57\% \pm 2\%$	320 Å

II. EXPERIMENTAL DETAILS

Samples were prepared at RT by magnetron sputtering at a base pressure of 10^{-8} mbar and 10^{-3} mbar Ar pressure. The thin films were grown on silicon wafer substrates using two separate magnetron guns. Neodymium and cobalt concentrations were controlled by changing the power in the magnetrons. The real concentration of the films was confirmed by electron induced fluorescence spectroscopy and their thickness by x-ray reflectometry. Table I shows a list of the samples characterized by XMCD giving their thickness and concentrations. All samples were prepared by codeposition of cobalt and neodymium with the exception of sample MNC5, which has almost the same nominal composition as sample NC5. It consists of a compositionally modulated structure created by the alternate deposition of Co and Nd with submonolayer thicknesses. We have observed that such a preparation method increases the PMA energy of our films. Structural differences between the codeposited and the modulated in composition films were detected by EXAFS [17]. The x-ray reflectivity of the multilayer films did not detect any superlattice structure. All the samples were protected with a 20-Å-thick aluminum capping layer. All of them were approximately 30 nm thick, close to the transcritical thickness above which stripe domains appear at 300 K for the concentration with the highest PMA [41]. The concentration of samples NC5 and MNC5 was chosen because it is close to that estimated to obtain the highest PMA in NdCo alloys [15,17]. The rest of the samples have concentrations above and below this reference concentration. In this way, the magnetism of the cobalt and neodymium subnetworks was studied in five different situations, which practically cover all the magnetic environments of interest: high (MNC5) and low

(NC5) PMA energy at the range of neodymium concentrations where the PMA is expected to be the highest, low neodymium concentration (NC10), high neodymium concentration (NC2), and paramagnetic (NC).

XMCD measurements were performed at beamline ID08 (now moved to ID32) at the ESRF (European Synchrotron Radiation Facility) using ≈100% circularly polarized x-ray light produced by an undulator, at the Co $L_{2,3}$ (780 eV) and Nd $M_{4,5}$ (980 eV) edges. The detection method used for the spectra acquisition was total electron yield (TEY). The strength of the applied magnetic field was 5 Tesla. The spectra were obtained at temperatures that varied from 10 K up to 300 K (RT). All spectra for each sample were measured at every temperature and sample orientation using right and left circularly polarized x rays with the magnetic field applied parallel and antiparallel to the direction of the x-ray beam making a total of eight spectra per measurement. The XMCD spectra obtained changing the polarization but keeping the magnetic field constant were indistinguishable from the obtained by inverting the orientation of the magnetic field and keeping the same polarization. All the spectra taken at each orientation and temperature but with different polarization or magnetic field direction were exactly the same at the nonresonant part of the spectra (mainly the pre-edge and post-edge regions), insuring that only the surface of the thin films was hit by the beam and a minimum of a spurious signal was introduced in the spectra.

The element-specific magnetic hysteresis loops of the magnetic moments of cobalt and neodymium were measured by fluorescence yield and the total electron yield detection in each sample using the variation in intensity of the Nd M_4 and the Co L_3 resonances with the applied magnetic field. They were measured at normal and grazing incidence (75°) and at different temperatures. There were no significant differences between the hysteresis loops taken with different detection modes. Therefore the signal obtained using the total electron yield should not be significantly influenced by surface effects [4].

III. EXPERIMENTAL RESULTS AND DISCUSSION

The first part of this section (part A) explains the application of the sum rules for the cobalt and neodymium subnetworks and their dependence on the angle of incidence. Part B shows the magnetic hysteresis loops of the samples measured by XMCD. They serve to indicate the approximate orientation of the magnetic easy axis and the possible partial decoupling between neodymium and cobalt magnetic moments in each sample. The last part of this section presents the results of the analysis for the spectra of cobalt (part C) and neodymium (part D): the magnitude of their spin and orbital moments and its dependence on the temperature and the magnetic field orientation. The procedure used to remove the background of the spectra and to correct saturation effects, which are specially important at grazing incidence, are explained in detail in the Appendix. A compilation with most of the XMCD spectra and hysteresis loops used in this analysis is shown in Ref. [42].

A. XMCD sum rules

The sum rules for the orbital component $\langle L_z\rangle_{\theta_i}$ projected on the magnetic field orientation (parallel to the incident beam) of the cobalt $3d$ and neodymium $4f$ bands are, respectively [19,21],

$$\frac{\int_{L_3+L_2} I^{\theta_i}_{\mathrm{XMCD}}(E)dE}{I_{\mathrm{XAS}}} = \frac{3}{2n_h}\langle L_z\rangle_{\theta_i}, \tag{1}$$

$$\frac{\int_{M_5+M_4} I^{\theta_i}_{\mathrm{XMCD}}(E)dE}{I_{\mathrm{XAS}}} = \frac{1}{n_h}\langle L_z\rangle_{\theta_i}. \tag{2}$$

The angle θ_i is measured with respect to the normal to the basal plane. n_h is the number of holes in the corresponding band. $I^{\theta_i}_{\mathrm{XMCD}}(E)$ is the XMCD spectrum obtained at the incidence angle θ_i after correcting the saturation effects [see Appendix, Eq. (A2)]. I_{XAS} is the integrated x-ray absorption resonance intensity averaged over all the orientations of the electric field with respect to the charge in the atomic volume [19,21,25].

The spin sum rule depends on an additional term, the projected component of the intratomic magnetic dipole moment $m^{\theta_i}_D$, which is proportional to the magnetic dipole operator $\langle T_z\rangle_{\theta_i}$ [29]. It measures the anisotropy of the spin density. Its value depends on how the charge couples to the spin which occurs differently in $3d$ cobalt than in $4f$ neodymium. In cobalt, the spin density follows the charge since the spin-orbit interaction is much weaker than the ligand crystal field. In this case, the intra-atomic magnetic dipole term represents the anisotropy of the charge due to bonding. This term vanishes when it is averaged over θ_i in cobalt making possible to determine the exact value of its total spin moment [21,43]. The angle-dependent spin sum rule for cobalt $3d$ electrons is

$$\frac{\int_{L_3} I^{\theta_i}_{\mathrm{XMCD}}(E)dE - 2\int_{L_2} I^{\theta_i}_{\mathrm{XMCD}}(E)dE}{I_{\mathrm{XAS}}} = \frac{1}{n_h}\left(2\langle S_z\rangle_{\theta_i} + 7\langle T_z\rangle_{\theta_i}\right). \tag{3}$$

The spin sum rule for the neodymium $4f$ band has to be substantially modified by core hole effects [44]. They alter the proportionality constant between the magnetic dipole term and the spin [21], which is more than five times increased, and the spin sum rule, which must be multiplied by a correction factor of $Q_X = 0.482$. Then, the spin sum rule for neodymium is

$$\frac{2\int_{M_5} I^{\theta_i}_{\mathrm{XMCD}}(E)dE - 3\int_{M_4} I^{\theta_i}_{\mathrm{XMCD}}(E)dE}{I_{\mathrm{XAS}}} = \frac{1}{n_h Q_X}\left(2\langle S_z\rangle_{\theta_i} + 6\langle T_z\rangle_{\theta_i}\right) = \frac{8.07}{n_h}\langle S_z\rangle_{\theta_i}. \tag{4}$$

The spin-orbit interaction in the neodymium $4f$ band is much stronger than the crystal field, coupling the charge tightly to the spin. This makes the intra-atomic magnetic dipole term constant at any magnetic field orientation angle, contrary to what occurs in cobalt. Sec. III D 2 will show that, unexpectedly, the magnetic dipole term changes with the angle θ_i, demonstrating that the neodymium $4f$ distribution charge is actually distorted by an anisotropic environment.

There is an additional sum rule of special significance in the present experiment, which is the orientation dependent

intensity sum rule [43,45]. This sum rule correlates the polarization dependent resonant absorbed intensity with the number of holes and the anisotropy of the charge density in the atomic volume:

$$I_{\mathrm{XAS}}^{\theta_i} = N_h + N_Q^{\theta_i}, \tag{5}$$

where N_h is the number of holes in the probed valence orbital and $N_Q^{\theta_i}$ is a quadrupole term derived from the anisotropy in the charge density of the atomic volume parallel to the polarization electric field, i.e., perpendicular to the angle of incidence, θ_i, of the beam. The intensity of the white line resonances at the angle of incidence θ_i, $I_{\mathrm{XAS}}^{\theta_i}$, is obtained by integration of the sum of the left and right circular polarization spectra after subtracting their nonresonant spectrum:

$$I_{\mathrm{XAS}}^{\theta_i} = \frac{1}{2}\int_{L_{3,2}(M_{5,4})} (\mu_+^{\theta_i}(E) + \mu_-^{\theta_i}(E) - 2\bar{\mu}(E))dE, \tag{6}$$

where $\bar{\mu}(E)$ is the nonresonant absorption coefficient. This sum rule is linked to the orientation-dependent spin sum rule through the dipole operator term, which depends on the spin density [43,45].

The number of holes, which is proportional to the I_{XAS} term in the XMCD rules for spin and orbital moment, is a necessary quantity to give absolute values of the spin and the orbital moments. In cobalt, this is obtained by averaging $I_{\mathrm{XAS}}^{\theta_i}$ over all the possible incident angles since the atomic cobalt charge is fixed to its local environment by the crystal field. This kind of average is not possible in neodymium since the charge follows the spin density [25,28]. We use a NdCo paramagnetic sample (sample NC) to make the average of I_{XAS} since its neodymium $4f$ quantization axis is randomly oriented with respect to the polarization electric field. A single measurement should be enough if the paramagnetic neodymium is isotropic or nearly isotropic. In this case, as in the case of a completely demagnetized sample, the value of I_{XAS} can be transferred to the other samples since the $4f$ orbital does not participate directly in the bonding and, therefore, there should be exactly the same number of holes independently of the sample composition or its magnetic state.

B. Hysteresis loops

Figures 1–3 show the magnetic hysteresis loops of the cobalt and neodymium subnetworks of samples NC5, MNC5, and NC. The loops of samples NC10 and NC2 were similar to those of sample NC5 and are shown in Ref. [42]. They were measured at two orientations of the magnetic field, perpendicular to the plane, $H_\perp$, and nearly parallel (75°) to the plane, $H_\parallel$, and at two different temperatures, 10 and 300 K. They are normalized to 1 at the field where the cobalt subnetwork reaches its saturation magnetization.

At RT, samples NC5, NC10 [42], and MNC5 have their easy axis in the plane. The saturation field of samples NC5 and MNC5 in the $H_\perp$ field orientation is very similar, of about 1 T, and it is close to 2 T in sample NC10. Sample NC is clearly paramagnetic at that temperature although some remaining cobalt shows a perceivable change in its magnetization only in the plane orientation, suggesting the presence of superparamagnetic cobalt regions.

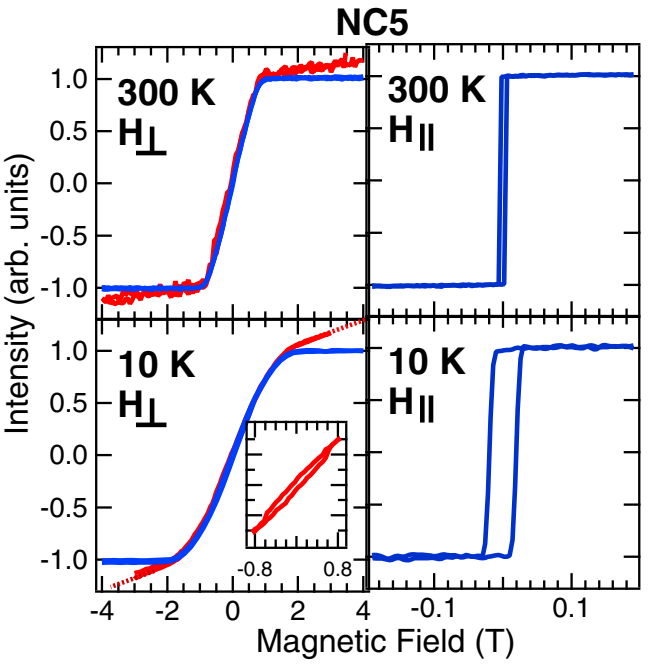

FIG. 1. Hysteresis loops of sample NC5 obtained measuring the variation in intensity of the Co L_3 edge (blue line) and the Nd $M_{4,5}$ edge (red line) at two different temperatures (10 and 300 K) and magnetic field orientations with respect to the normal to the sample. The hysteresis loop of the neodymium subnetwork has been linearly extrapolated from 3 to 4 T. The inset shows in detail the coercivity in the $H_\perp$ field orientation. Note that the decoupling between neodymium and cobalt magnetization observed at high fields increases at low temperature.

At 10 K, samples NC5 and NC10 [42] increase their coercive field in the plane. The saturation field in their out-of-plane hysteresis loop increases, most obviously in sample NC5. There is also an increase in their coercive field for this orientation of the order of 0.2 T (see insets) together with a slower approach of the magnetization to its saturation than at RT. These kind of loops are present in films with weak stripe domains [46,47]. This indicates that the magnetic anisotropy of these films has a weak, but non-negligible, perpendicular component.

The presence of a macroscopic perpendicular magnetic anisotropy at 10 K is more evident in sample MNC5, signaling this sample as the one with the highest PMA of all those measured in this experiment. Its hysteresis loops collected at 10 K show typical features related to magnetic domains with their magnetization pointing out of the plane. The shape of the loop obtained with the $H_\perp$ field orientation is typical in the formation of magnetic bubbles. The measurement in the $H_\parallel$ field orientation is what is called a transcritical loop. This kind of loop appears above a critical thickness whose size depends on the magnetization and the PMA energy of the film [6,41,46–48]. A rough estimation of the PMA energy in this sample based on its XMCD hysteresis loops and magnetization yields a value not far from 1.3×10^6 J m^{-3}, which is similar to that obtained using a more precise method in a similar but thicker sample [17,41,49]. This energy is about four times smaller than the one measured in crystalline $NdCo_5$

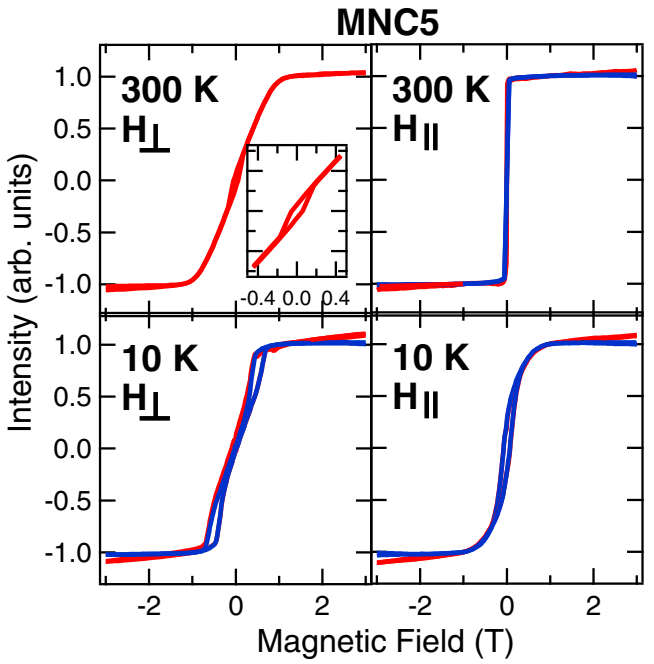

FIG. 2. Hysteresis loops of sample MNC5 obtained measuring the variation in intensity of the Co L_3 edge (blue line) and the Nd $M_{4,5}$ edge (red line) at two different temperatures (10 and 300 K) and magnetic field orientations with respect to the normal to the sample. Only the neodymium subnetwork was measured at 300 K and normal incidence. The inset shows in detail the coercivity in the $H_\perp$ field orientation at this temperature. Note that the decoupling between neodymium and cobalt magnetization observed at high fields increases at low temperature.

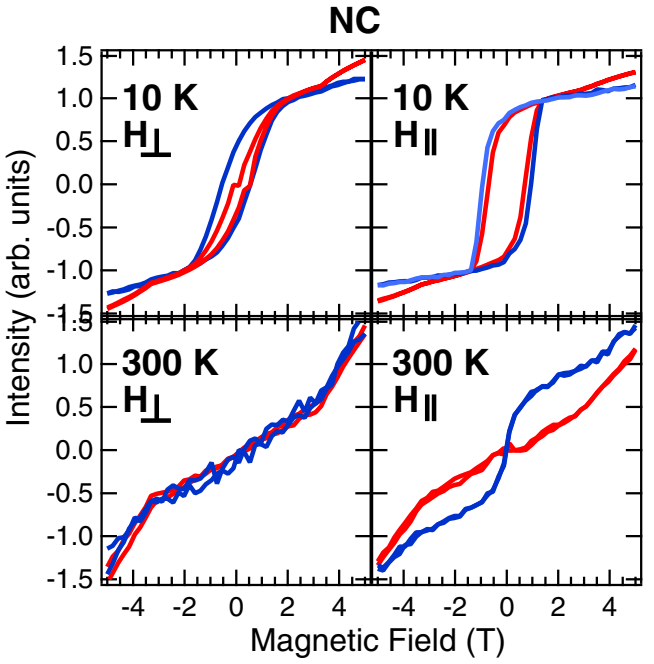

FIG. 3. Hysteresis loops of sample NC obtained measuring the variation in intensity of the Co L_3 edge (blue line) and the Nd $M_{4,5}$ edge (red line) at two different temperatures (10 and 300 K) and magnetic field orientations respect to the normal to the sample.

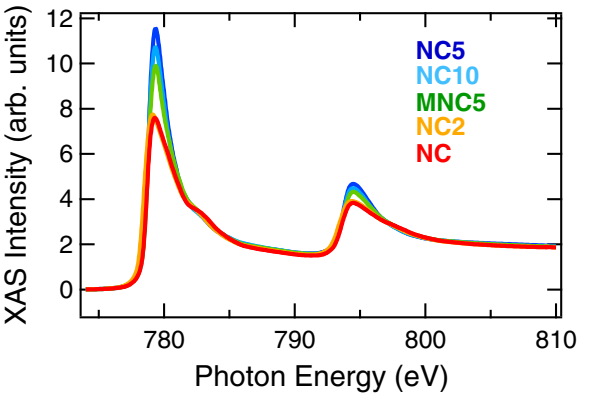

FIG. 4. Angle averaged Co $L_{2,3}$ absorption spectra obtained at 10 K.

at 10 K [50], and more than twice the PMA energy measured in amorphous NdCo alloys in this range of concentrations [15].

The hysteresis loops of sample NC2 [42] at 10 K are similar to the observed in samples NC5 and NC10 at the same temperature, with the easy axis in the plane and a saturation field in the out-of-plane orientation of about 2 T. The most significant changes in sample NC from RT to 10 K are the presence of coercive fields at both orientations. They are different for each subnetwork, specially in the out-of-plane orientation. The presence of large coercive fields is typical in amorphous RE-TM alloys with uniaxial random anisotropy. It is expected to arise in these kind of alloys when the local anisotropy in the RE sites overcomes the exchange interaction between the RE and the TM [51,52].

There exist differences in the magnetization between the cobalt and neodymium subnetworks in all the samples. The magnetization of neodymium presents a significant susceptibility at fields where the magnetization of cobalt is already saturated. This effect increases at low temperatures and it is very clear in sample NC5. The decoupling between the magnetization of the two subnetworks indicates the presence of a fraction of neodymium that is very weakly or not magnetically interacting with cobalt, which is, consequently, paramagnetic [53]. The paramagnetic character of this neodymium phase is evidenced because its magnetic susceptibility increases at low temperatures. The presence of this phase in alloys with such a relatively large proportion of cobalt versus neodymium concentration, as in sample NC5, can only be explained if they are not homogeneous. We will show that the results derived from the analysis of the XMCD spectra confirms the nonhomogeneity of the films, previously detected by EXAFS [17], and the presence of a significant concentration of neodymium magnetically decoupled to cobalt, i.e., paramagnetic.

C. Cobalt

1. Variation of the magnetic moment with Nd concentration

Figure 4 shows the unpolarized spectrum of Co $L_{2,3}$ for each of the analyzed samples obtained at 10 K and averaged in angle. The main changes are in the maximum intensity of the L_3 and L_2 resonances. Their reduction is stronger in the samples with the higher neodymium concentration. However, this reduction is not strictly proportional to the concentration.

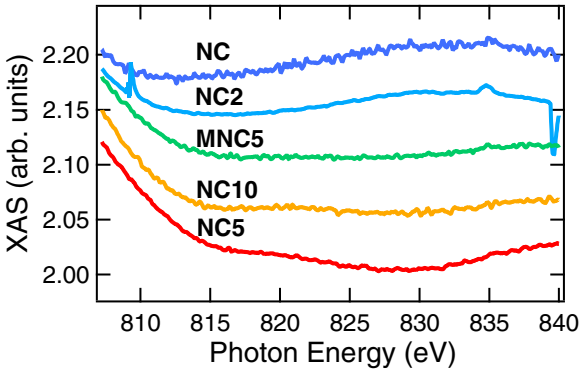

FIG. 5. Tails of the angle averaged Co $L_{2,3}$ absorption spectra obtained at 10 K.

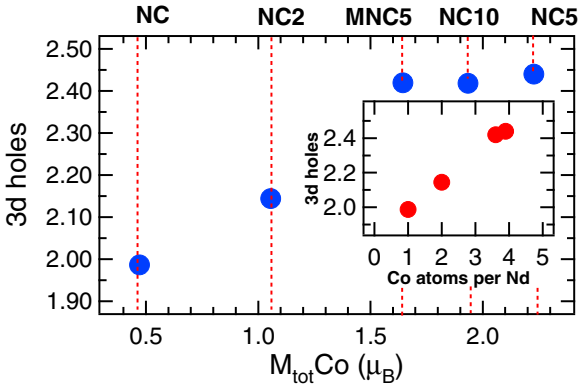

FIG. 6. Magnetic moment of cobalt as a function of the number of 3*d* holes per atom measured at 10 K by XMCD.

Sample NC5, with a concentration of neodymium of 20%, happens to have the highest intensity whereas that of sample NC10, with 9% of neodymium, is discernibly lower. There is also a broad component centered at about 783 eV, which is more intense in samples NC2 and NC. All these changes are relatively small between samples NC5, NC10, and MNC5, but significantly stronger when compared to samples NC2 and NC. Figure 5 show the tails of the Co $L_{2,3}$ spectra of the samples. This part of the spectra is related to EXAFS and, possibly, to collective electron excitations. The extension of the spectra does not contain enough oscillations to make a quantitative analysis of the structure. But it serves to state that the structure of samples NC5, NC10, and MNC5 are similar and certainly different from the structure of samples NC2 and NC. Our previous EXAFS analysis in samples with concentrations and magnetic properties similar to those of sample MNC5 showed that cobalt has a short-range order similar to cobalt fcc with their cobalt-cobalt bond length shrinked 4% with respect to fcc cobalt, from 2.50 to 2.40 Å. We deduced that the structure for most of the cobalt is similar in NC5 and NC10 based on Fig. 5 and, perhaps, more ordered in sample NC5 given the relatively stronger amplitude of these oscillations.

The averaged intensity I_{XAS} of the $L_{2,3}$ spectrum of cobalt is proportional to the density of 3*d* holes, which is reduced by charge transfer and hybridization with the valence band states of neodymium. The proportionality constant between I_{XAS} and the number of 3*d* holes is chosen assuming that the total number of 3*d* holes in the sample with the highest value of I_{XAS} (sample NC5) is 2.44, a bit lower than the expected in pure cobalt (2.49). Such a specific number of holes has been obtained taking into account that the estimated proportion of neodymium atoms bonded to cobalt in sample NC5 is about 25% (the details of this estimation are given in Sec. III D 1) and the expected transferred charge per neodymium atom is, theoretically, not higher than 1 electron [54]. This quantity might be overestimated since indirect experimental measurements suggest values lower than 0.5 electrons [55].

Figure 6 shows the variation in the number of 3*d* holes per cobalt atom as a function of the cobalt magnetic moment in each sample using the mentioned reference for the number of holes. There is a direct correlation between both quantities with two different regions. In the region defined by samples NC5, NC10, and MNC5, the relatively large decrease in the cobalt magnetic moment requires very little change in the number of holes. The decrease in the magnetic moment and the number of holes is faster for samples with neodymium concentrations higher than in sample MNC5. In this region, the reduction in the number of holes is practically linear with the amount of cobalt atoms per neodymium. This is shown in the inset of Fig. 6. It is deduced from this that the highest charge transfer per neodymium atom is less than 0.7 electrons and it occurs in sample NC2. Since charge transfer is done through bonding, this sample should have the highest number of cobalts bonded to neodymium of all the samples.

Figure 7 plots the magnetic moment of neodymium versus the magnetic moment of cobalt for each sample determined by XMCD at 10 K. There is an inverse correlation between both quantities. The magnetic moment of cobalt decreases as it bonds to neodymium whereas the effect in the magnetic moment of neodymium is the opposite, as expected [56,57]. This correlation is quasilinear for samples NC10, NC5, and MNC5 whose change in the number of 3*d* holes is small. Samples NC2 and NC seem to be out of this relation due to the saturation (NC2) or reduction (NC) of the neodymium magnetic moment. This is because the magnetic moment of neodymium depends on the total magnetic moment of cobalt. In these samples, the concentration of cobalt-neodymium bonds is larger, the number of 3d holes is lower and the exchange between cobalt atoms is weaker, reducing the strength of the indirect exchange with neodymium. Nevertheless, note that their neodymium to

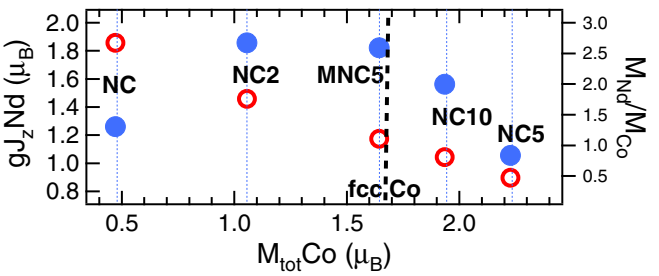

FIG. 7. Left axis, blue dots: magnetic moment of neodymium per atom vs the magnetic moment of cobalt per atom measured at 10 K by XMCD. Right axis, red circles: neodymium to cobalt magnetic moment ratio.

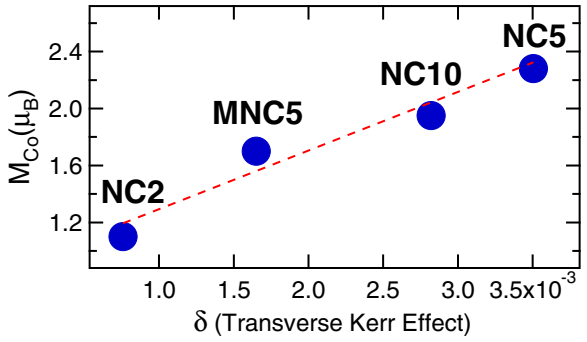

FIG. 8. Magnetic moment of cobalt per atom measured by XMCD vs the transverse Kerr effect signal δ (change in the reflectivity) measured in samples NC5, MNC5, NC10, and NC2 at RT.

cobalt magnetic moment ratio, shown in the same figure, is much higher than in the other samples, indicating that the magnetic coupling of neodymium to cobalt is more effective in them. Note also that the sample with the highest neodymium magnetic moment, sample NC2, is the sample with the highest cobalt coordination per neodymium atom, whereas the sample with the highest number of holes, sample NC5, is the sample with the lowest neodymium magnetic moment and the highest cobalt magnetic moment. Therefore there is a clear correlation between the number of $3d$ holes and the magnetic moment of neodymium in agreement with the fact that the magnetic polarization of the $4f$ spin is done by means of the $3d$ cobalt electrons.

On the other hand, there is no correlation between the concentration of the samples and the expected neodymium magnetic moments. If the distribution of cobalt and neodymium was homogeneous, the lowest neodymium to cobalt magnetic moment ratio should be found in sample NC10 and the highest in samples NC2 and NC, whereas it should be the same in samples NC5 and MNC5. This is a strong indication that there is a substantial proportion of neodymium atoms that are not bonded to cobalt giving rise to inhomogeneous alloys. In this sense, the plot in Fig. 7 might be understood as a representation of the level of segregation in each sample, being the highest in sample NC5 and the lowest in samples NC2 and NC. More details about the estimated amount of neodymium bonded to cobalt in each sample will be given in Sec. III D 1.

Remarkably, the magnetic moment of cobalt in sample NC5 is significantly higher (2.2 μ_B) than in sample NC10 which, because of its low content in neodymium, should have a cobalt moment closer to that of pure cobalt (1.7 μ_B). To support this surprising result, we analyzed the same samples by transverse Kerr effect (TKE). The cross section of the TKE effect is directly proportional to the cobalt magnetic moment with a negligible cross section for the magnetic moment of the RE. Figure 8 displays the plot of the magnetic moment of cobalt of all the analyzed samples measured by XMCD versus their TKE effect at RT. There is a linear correlation between both quantities, confirming the variations in the cobalt magnetic moment between samples and, therefore, the enhanced magnetic moment of cobalt in NC5.

An enhancement of the spin and orbital moment of cobalt of the same magnitude as that presented in sample NC5 has

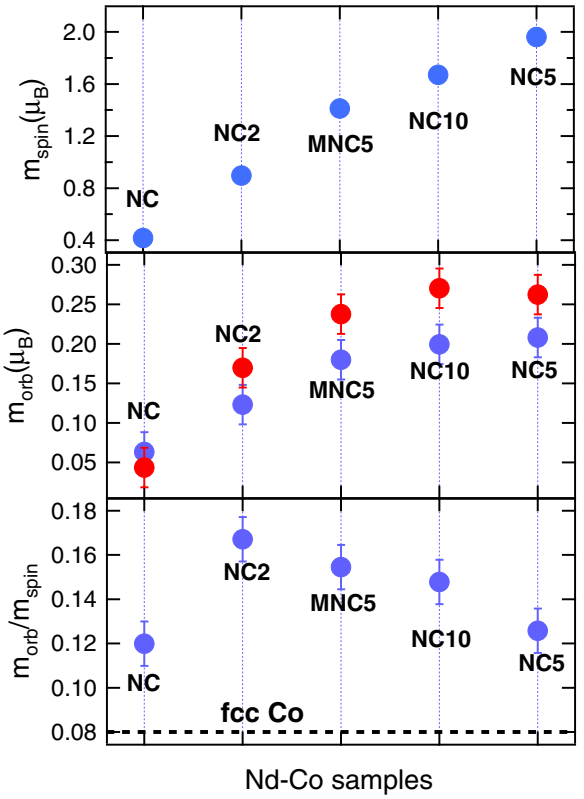

FIG. 9. Spin magnetic moment, m_s (top), orbital magnetic moment m_o (middle), and ratio m_o/m_s of cobalt of each sample measured at normal incidence and at 10 K (blue solid dots). Samples are ordered by their total cobalt magnetic moment, from low (NC) to high (NC5) moment. The red solid dots in the middle panel are the orbital moments m_o measured at 10 K and at grazing incidence (75°).

been registered in cobalt clusters embedded in gold [58]. The enhancement in the spin moment was attributed to a higher localization of the $3d$ cobalt states due to the small size of the clusters, of the order of 7 nm or below, and their lack of hybridization with the $5d$ states of gold. This is expected in sample NC5 due to the phase segregation, the short range order of the cobalt subnetwork and the observed poor bonding of cobalt to neodymium. The significant cobalt bond contraction measured in these samples by EXAFS [17], of the order of 4%, is another indication of the presence of cobalt clusters since it is expected to occur in low coordinated cobalt [59,60]. The observed fast decrease in the cobalt magnetic moment without significant changes in the number of $3d$ holes agrees with this particular distribution of cobalt. Therefore the decay in the magnetic moment will be produced not only by cobalt bonding to neodymium but by destroying the special conditions that give rise to the enhancement of the cobalt moment.

2. *Variation of the measured orbital and spin moment of cobalt with the magnetic field orientation*

Figure 9 shows the values obtained by XMCD at 10 K of the spin moment m_s, orbital moment m_o, and the ratio between both quantities m_o/m_s for all the samples. The change in m_o varies with the orientation of the applied field, being larger near the surface plane (red solid dots) than along the normal

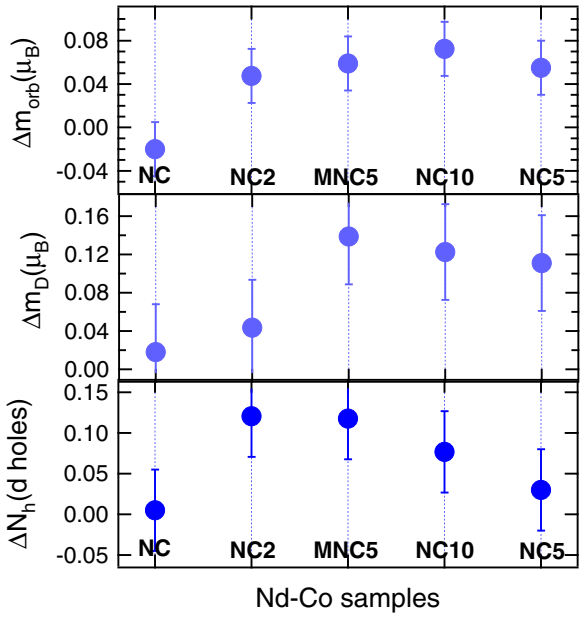

FIG. 10. Variation between grazing incidence (75°) and normal incidence of the orbital magnetic moment Δm_o (top), the intratomic dipole magnetic moment Δm_D (middle), and the number of d holes of cobalt at 10 K in all the analyzed samples. Samples are ordered by their total cobalt magnetic moment, from low (NC) to high (NC5) moment.

direction (blue solid dots). The plots show that the decrease is faster in m_s than in m_o, with the exception of sample NC, which might have to do with an increasing localization in the magnetic moment of cobalt from sample NC5 to sample NC2. The value of the orbital moment in MNC5, NC5, and NC10 is of about 0.25 μ_B, larger than in hcp cobalt (≈0.154 μ_B). This value is close to that found in clusters of cobalt embedded in gold [58] and also in RE-TM compounds [61].

The orbital moment is anisotropic in all the samples being larger near the basal plane than normal to the plane except in sample NC whose orbital moment decreases near the plane. This is shown in Fig. 10. The same figure shows the variations in the orbital moment Δm_o^{75-0}, the intratomic magnetic dipole moment $\Delta m_D^{75-0} = 7\mu_B \Delta\langle T_z\rangle_{75-0}$ and the number of d holes ΔN_h^{75-0} between grazing and normal incidence. All the three parameters are reasonably well correlated. A higher number of d holes at grazing incidence (higher value of I_{XAS}^{75}) means that the density of 3d holes is higher in the direction near to the normal to the sample. This is what happens in a free monolayer of cobalt [29]. If we compute the hole occupancy per 3d orbital of the majority ↓ and minority ↑ spin subbands in the direction parallel $N_{\downarrow,\uparrow}^{\parallel}$ and perpendicular $N_{\downarrow,\uparrow}^{\perp}$ to the sample following Stöhr [29], we obtain $N_{\downarrow}^{\parallel} = 0.07$, $N_{\uparrow}^{\parallel} = 0.4$, $N_{\downarrow}^{\perp} = 0.1$, and $N_{\uparrow}^{\perp} = 0.45$ in the sample NC10 at 10 K. These values are not too far from those obtained in a free monolayer: $N_{\downarrow}^{\parallel} = 0.1$, $N_{\uparrow}^{\parallel} = 0.38$, $N_{\downarrow}^{\perp} = 0.04$, and $N_{\uparrow}^{\perp} = 0.47$. It is apparent that the magnetic anisotropy in the plane of cobalt should be caused more by an anisotropy in the arrangement of cobalt atoms and less directly caused by the bonding between cobalt and neodymium, at least in the samples with low neodymium content due to their already mentioned large phase segregation.

A rough estimation of the magnetocrystalline anisotropy energy of the cobalt subnetwork can be made for each sample assuming that it is entirely due to the variation in the spin-orbit energy, ΔE_{so}. This is proportional to the change in the orbital moment between the hard and the easy axis, Δm_o, following the relation proposed by Bruno: $\Delta E_{so} = C\xi\Delta m_o/4\mu_B$ [34]. A correction factor C must be applied since the energy calculated using this expression can be up to 20 times bigger than the value measured macroscopically [29]. Then, the in-plane magnetic anisotropy energy estimated for samples NC5, MNC5, and NC10 due to the cobalt subnetwork is of about 0.4×10^6 J m^{-3}, using the same correction factor as used in cobalt on gold of $C = 0.05$ [29], and considering a spin-orbit coefficient ξ of 70 meV [62]. This energy is comparable to the shape energy calculated for samples NC5 and NC10 using the magnetic moments measured by XMCD and assuming a demagnetizing field of an ideal thin layer. This energy is $\approx 0.8-0.6\times10^6$ J m^{-3}. The in-plane magnetocrystalline anisotropy energy $E_{M\parallel}$ can be also estimated from the saturation magnetic field obtained in the out-of-plane hysteresis loops (H_s) and the calculated demagnetizing field: $E_{M\parallel} = \frac{1}{2}(H_s - H_D)M$. It yields a value of 0.3×10^6 J m^{-3} for samples NC5 and NC10 that agrees quite well with the obtained from the Bruno model using the mentioned correction factor. This does not work so well for sample NC2. Its magnetization is smaller giving rise to a shape anisotropy of only $\approx 0.3\times10^6$ J m^{-3}. Its magnetocrystalline anisotropy energy estimated from the out-of-plane hysteresis loop [42] is similar to that obtained in samples NC5 and NC10. However, the correction factor that must be used in the Bruno model to match this magnetic anisotropy energy must be 1.5 times higher ($C = 0.07$). It is like as if the in-plane magnetocrystalline anisotropy of cobalt was more effective in this sample. This correction factor might be even higher since its neodymium subnetwork appears to have its easy axis in the perpendicular direction (see Sec. III D 2). If the energy of this perpendicular magnetic anisotropy is similar to that of sample MNC5 (1.3×10^6 J m^{-3}), the correction factor becomes $C = 0.2$ [58]. Such variations in the correction factor C indicate that the orbital moment is not the only important element to take into account to determine the magnetic anisotropy in metallic alloys.

D. Neodymium

1. *Variation of the neodymium magnetic moment with the temperature*

The variation with temperature of the angular moment of neodymium projected in the measured direction, J_z, is shown in Fig. 11 for samples NC5, NC10, and MNC5. These are the samples whose Curie temperature is well above RT. The variation of their cobalt magnetic moment with temperature from 10 K to RT, shown in Fig. 12, is less than 5%. The thermal variation of the neodymium angular moment is related to the magnetic interaction that takes place at the RE whose magnitude can be estimated using the random anisotropy model, also called HPZ model by the name of their authors [51,63]. According to it, the orientation of the angular moment

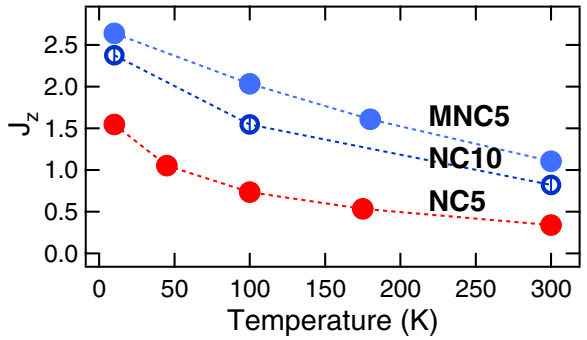

FIG. 11. Variation with the temperature of the component of the angular moment of neodymium projected in the direction of the applied field, J_z, for samples MNC5 (blue dots), NC10 (empty blue dots), and NC5 (red dots). The applied field is applied normal to the samples.

J of the $4f$ electrons of neodymium depends on the local crystal field and the effective indirect exchange with cobalt, this latter expressed as a molecular field acting on the angular moment. The magnetic exchange between neodymium atoms is of a much smaller magnitude and it is usually not taken into account. The expression for the energy of a neodymium atom in this model is

$$E = -D(g\mu_B J)^2(\vec{u_J}\cdot\vec{u_\alpha})^2 - g\mu_B J\, H_{\text{eff}}\cos\theta, \qquad (7)$$

where D is the coefficient for an uniaxial crystal field averaged over all the possible crystal fields in the alloy. It is assumed to be constant with the temperature. H_{eff} is the sum of the indirect exchange molecular field H_{exch} between neodymium and cobalt, and H_o, the applied magnetic field. The Landé factor g used for neodymium is 0.726. $\vec{u_J}$ and $\vec{u_\alpha}$ are the unit vectors of the angular moment and the crystal field axis, respectively, where

$$\vec{u_J}\cdot\vec{u_\alpha} = \sin\alpha\sin\theta\cos\varphi + \cos\alpha\cos\theta, \qquad (8)$$

where α is the angle formed between the easy axis of the crystal field and the direction of the applied field, θ is the angle between the angular moment J and the applied field, and φ is the azimuthal orientation of the angular moment. We used the classical approximation since the angular moment in Nd ($J = 4.5$) is high enough to expect small differences with respect to a quantum treatment. Therefore the thermal

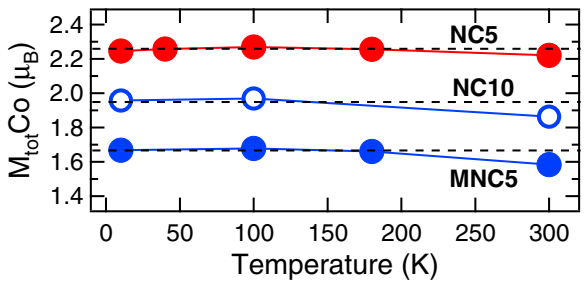

FIG. 12. Variation with the temperature of the angle averaged cobalt magnetic moment of samples MNC5 (blue dots), NC10 (empty blue dots), and NC5 (red dots). The dashed lines are a guide to the eye.

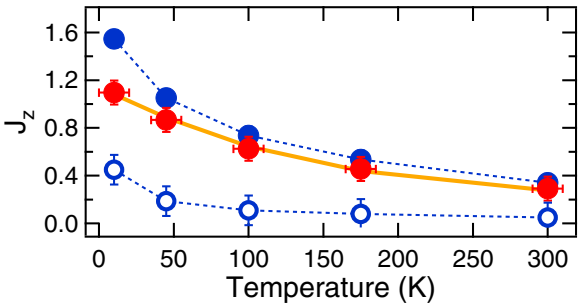

FIG. 13. Variation with the temperature of the component of the angular moment of neodymium projected in the direction of the applied field, J_z for sample NC5 (blue dots), the speromagnetic contribution deduced from the hysteresis loops (empty blue dots), and the remaining asperomagnetic contribution (red solid dots). The dashed lines are a guide to the eye. The thick line is the resulting fit using the HPZ model.

average for the projected angular moment of neodymium in the direction of the applied field when the easy axis of the crystal field is oriented in the angle α, $\langle J_z\rangle_\alpha$, is

$$\langle J_z\rangle_\alpha = \frac{\int_0^{2\pi}\int_0^{\pi} J\cos\theta\,\exp(-E/k_BT)\sin\theta d\theta d\varphi}{\int_0^{2\pi}\int_0^{\pi}\exp(-E/k_BT)\sin\theta d\theta d\varphi}. \qquad (9)$$

The experimental value of J_z should be the average of $\langle J_z\rangle_\alpha$ over all the possible orientations α of the easy axis of the crystal field. If we suppose that the distribution of the uniaxial crystal field environments is nearly isotropic,

$$\langle J_z\rangle = \int_0^{\pi/2}\langle J_z\rangle_\alpha\sin\alpha d\alpha. \qquad (10)$$

An attempt to fit the data of Fig. 11 using this model yields unsatisfactory results (not shown), mainly due to the too small values of the measured magnetic moments. In the HPZ model, any reduction in the projected magnetic moment of neodymium ($g\mu_B J_z$) with respect to its highest possible value ($g\mu_B J$) is caused by the crystal field. This means that the thermal variation of $g\mu_B J_z$ should become smaller as the temperature approaches 0 K. This is the opposite to what is observed in our films, specially for the case of sample NC5. Actually, the magnetic moment measured in this sample at 10 K is significantly lower than the lowest value of $g\mu_B J_z$ that the HPZ model could predict at 0 K, which is $g\mu_B J/2$ [51,64].

The low values of the magnetic moment of neodymium can be explained assuming the presence of two neodymium magnetic phases, of which only one of them is magnetically coupled to cobalt. The variation of the neodymium magnetic moment with the temperature in this magnetically coupled phase, also called asperomagnetic, should be reproduced using the HPZ model. The other phase, named speromagnetic, has a very weak or no magnetic interaction with cobalt [57,65]. Since this phase is paramagnetic, its contribution is higher at lower temperatures. This component has to be responsible of the observed decoupling between the magnetization of the cobalt and neodymium subnetworks in the hysteresis loops.

Figure 13 shows the speromagnetic and asperomagnetic contributions in sample NC5 extracted from its hysteresis loops. A similar separation was done in samples NC10 and

TABLE II. Parameters used to simulate the thermal variation of the magnetization of the neodymium subnetwork using the HPZ model and assuming the presence of two magnetic phases (see the text). H_{exch} and $g\mu_B JD$ are the Nd-Co molecular exchange field and the crystal field of the asperomagnetic phase. η_{HPZ} is the guessed concentration of the asperomagnetic phase.

Sample	H_{exch}	$g\mu_B JD$	η_{HPZ}
NC5	105 ± 1 T	0 ± 16 T	$25 \pm 1\%$
NC10	130 ± 1 T	20 ± 25 T	$40 \pm 1\%$
MNC5	194 ± 1 T	89 ± 25 T	$60 \pm 1\%$

MNC5. The fit of the asperomagnetic phase data is done using three variables: the Nd-Co exchange molecular field H_{exch}, the uniaxial crystal field coefficient D, and the concentration of the asperomagnetic phase. The fits are not statistically reliable in sample NC10 because the number of variables to fit is the same than the number of points. The most unreliable value for this sample was the crystal field coefficient. The resulting parameters of the fits are shown in Table II.

Neodymium atoms in sample MNC5 have the strongest magnetic interaction with cobalt. The lowest interaction is found in sample NC5. The energy of the indirect exchange with cobalt, $\mu_B H_{\text{exch}}$, ranges from 6 meV in sample NC5 to 12 meV in sample MNC5. The crystal field in sample MNC5 has an energy $g\mu_B^2 JD$ of less than 6 meV. The apparent absence or very reduced crystal field in samples NC5 and NC10 might be caused by a still non-negligible contribution of neodymium atoms weakly interacting with cobalt. The guessed concentrations of the asperomagnetic phase in each sample are surprisingly low, specially in sample NC5, which is of only 25% of the total number of neodymium atoms in the alloy. The concentration of the speromagnetic phase for each sample agrees with the level of phase segregation deduced from the plot of the cobalt magnetic moment versus neodymium magnetic moment shown in Fig. 7, which is highest in sample NC5 and lowest in sample MNC5.

The observed phase segregation is in qualitative agreement with that expected from the Nd-Co phase diagram [40]. The formation of amorphous alloys is a very unstable process by definition. In this case, the film deposition process is not fast and cold enough to quench the atoms as the arrive to the substrate. The diffusion lengths are long enough to make cobalt and neodymium meet at the eutectic concentrations forming regions richer in neodymium within a matrix rich in cobalt. For some reason, this particular process was more effective in sample NC5. These neodymium rich regions gives rise to the speromagnetic phase. They are the most disordered regions since their concentration corresponds to an eutectic point of the Nd-Co phase diagram. This high structural disorder might explain the susceptibility of the speromagnetic neodymium in these films, which is lower than the observed for metallic neodymium [53]. The magnetic interaction between neodymium atoms is believed to be mediated by their 5*d* orbitals [54,66], whose overlap and delocalization decreases with disorder, consequently decreasing the intensity of their magnetic interaction.

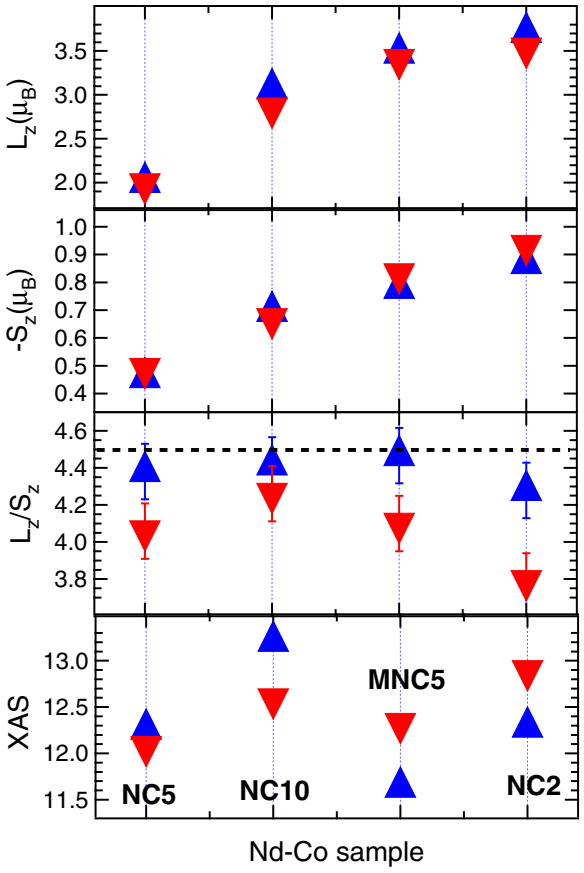

FIG. 14. (Top) Variation of the projected orbital component L_z and spin component S_z of neodymium (top panels) with the orientation of the applied field (0°: blue up arrow; 75°: red down arrow). (Bottom) Variation of the ratio L_z/S_z and the intensity of the absorption spectra, XAS, of neodymium with the orientation of the applied field (0°: blue up arrow; 75°: red down arrow). Samples are ordered by their neodymium magnetic moment, from low (NC5) to high (NC2).

2. *Variation of the measured neodymium magnetic moment with the magnetic field orientation*

Figure 14 shows the variation of the orbital moment (L_z), the spin (S_z), the ratio (L_z/S_z), and the Nd $M_{4,5}$ absorbed intensty ($I_{\text{XAS}}^{0,75}$) measured with the applied magnetic field and the x-ray incidence angle normal to the sample (blue up arrow) and at 75° away from the normal (red down arrow) in samples NC10, NC5, MNC5, and NC2 at 10 K. The values of L_z are always higher at normal than at 75°. This is more clear in samples NC10 and NC2. This difference is small in NC5 and MNC5. However, the value of S_z does not follow the same trend. It is lower in sample NC10 only. This difference between the variation in L_z and S_z is emphasized by making their ratio L_z/S_z. The sample with the lowest difference in their L_z/S_z ratio is sample NC10 and the one with the highest is sample NC2. The highest ratios are obtained always at normal incidence. They are close to 4.5, which is below the theoretical value expected in an isolated Nd atom after Teramura *et al.* calculations [44], which is 4.75. The differences between the L_z/S_z ratios between 0° and 75°

orientations are small, between 4% and 10%. However, they are systematically repeated for any measured temperature.

The variation of the L_z/S_z ratio with the angle of incidence indicates that the dependence of S_z with the magnetic dipole moment $\langle T_z \rangle$ is not constant, as assumed in Eq. (4), but it depends on the magnetic field orientation angle θ_i. A change with the angle θ_i of only the spin moment without a modification of $\langle T_z \rangle$ is not possible since that will mean that the exchange interaction in the planar direction is higher or comparable in energy to the spin orbit interaction, what is unjustified in a rare earth such as neodymium.

As already discussed in Sec. III A, the spin sum rule and the sum rule for the intensity are correlated because both depend on the angular distribution of the charge density in the atomic volume [29,43]. This correlation is visible in our data in Fig. 14. I^{75}_{XAS} is smaller than I^{0}_{XAS} in samples NC10 and NC5, which are the two samples whose spins S^{75}_z are smaller or nearly equivalent to normal incidence. The other two samples have their highest spin moment and their highest intensity taking place at the plane orientation. Actually, we observe such a correlation at any temperature. We have checked it by dividing the value of the XMCD signal at each orientation angle by its related angle-dependent intensity $I^{\theta_i}_{\mathrm{XAS}}$ instead of by its average value I_{XAS}, as should be done [see Eq. (4)]. This completely suppresses the variations of S_z with the angle in all the samples at any temperature.

Therefore the variations in the ratio L_z/S_z between normal and near to the plane orientation are due to differences in the distribution of the charge between both orientations. To understand the variations that occur in each of the analyzed samples, it is important to understand what measures $I^{\theta_i}_{\mathrm{XAS}}$ in samples where the angular moment $\vec{J}$ is not completely aligned to the applied magnetic field as in this case. If a particular neodymium atom has its angular moment oriented at an angle α with respect to the direction of the incident, circularly polarized, x-ray beam (which is parallel to the applied magnetic field), then (see the calculation in Ref. [42])

$$I^{\theta_i}_{\mathrm{XAS}} = [I^{\theta_i}_{\perp} + I^{\theta_i}_{\parallel}] + [I^{\theta_i}_{\perp} - I^{\theta_i}_{\parallel}]\,\cos^2\alpha_{\theta_i}, \tag{11}$$

where $I^{\theta_i}_{\perp}$ and $I^{\theta_i}_{\parallel}$ are the intensities measured with the electric field perpendicular and parallel to the angular moment of neodymium, θ_i being the orientation of the applied magnetic field. The total probed charge must be constant, i.e., independent of the angle of incidence chosen in the experiment. Therefore the following relation between $I^{\theta_i}_{\perp}$, $I^{\theta_i}_{\parallel}$ and the averaged intensity I_{XAS} must be fulfilled:

$$3I_{\mathrm{XAS}} = 2I^{\theta_i}_{\perp} + I^{\theta_i}_{\parallel}. \tag{12}$$

Then, Eq. (11) can be expressed as a function of I_{XAS} and $I^{\theta_i}_{\perp}$:

$$I^{\theta_i}_{\mathrm{XAS}} = \left(3\cos^2\alpha_{\theta_i} - 1\right)I^{\theta_i}_{\perp} + 3I_{\mathrm{XAS}}\left(1 - \cos^2\alpha_{\theta_i}\right). \tag{13}$$

The difference between the intensities taken at $\theta_i = 0^\circ$ and $\theta_i = 75^\circ$, $\Delta I^{75-0}_{\mathrm{XAS}}$, yields terms that are a function of $\cos^2\alpha_0$ and $\cos^2\alpha_{75}$, which are substituted by $J^2_{z_{0,75}}/J^2$:

$$\Delta I^{75-0}_{\mathrm{XAS}} = (3\cos^2\alpha_0 - 1)\Delta^{75-0}_{\perp} + \frac{J^2_{z_0} - J^2_{z_{75}}}{J^2} I^{75}_{\mathrm{XMLD}}, \tag{14}$$

where

$$\Delta^{75-0}_{\perp} = (I^{\alpha_{75}}_{\perp} - I^{\alpha_0}_{\perp}) \tag{15}$$

and

$$I^{75}_{\mathrm{XMLD}} = (I^{\alpha_{75}}_{\parallel} - I^{\alpha_{75}}_{\perp}), \tag{16}$$

where I^{75}_{XMLD} is identical to the definition of magnetic linear dichroism of second class [67] when it is obtained at grazing incidence. The first term of expression (14) is the difference in the density of empty states between the direction near to normal to the sample and in the plane with the magnetic field applied in the transverse direction. Therefore it measures the difference in the distortion of the $4f$ charge in the direction transverse to that of the magnetic field when it is applied near parallel (75°) and perpendicular to the plane (0°). This is the definition of the sum rule expressed in Eq. (5) for the variation of the intensity with the angle. The second term is a modification to this sum rule when the magnetic moment is not magnetically saturated in both directions since it depends on the difference $J^2_{z_0} - J^2_{z_{75}}$. If the magnetic anisotropy is perpendicular to the plane, $J^2_{z_0} > J^2_{z_{75}}$.

Experimentally, we have seen than the intensity in the paramagnetic material is smaller than in the other alloys with $J_z > 0$. Because of the relation (11), $I^{\alpha}_{\parallel} < I^{\alpha}_{\perp}$. Then, $I^{75}_{\mathrm{XMLD}} < 0$, and the second term in the equality (14) is negative when the easy axis is perpendicular to the plane. The first term will be positive instead. The distribution of charge in neodymium has an oblate form. Therefore it is expected that the density of unocuppied states is reduced in the direction transverse to the magnetic field when this is applied along the easy axis, which in this case is considered normal to the plane, than perpendicular to it. The stronger the deformation the higher this term will be. Both terms are correlated with the two terms of the spin sum rule, S_z and T_z. The second term in (14) gets more negative if S_z is smaller in the direction of the hard axis. And T_z increases in the direction of the hard axis as the distortion in the charge is increased with respect to the easy axis. Therefore sample NC10, whose easy axis is normal to the plane because L_z is higher in this direction, should be the sample with the lowest value in T_z because it dominates the second term in the quantity $\Delta I^{75-0}_{\mathrm{XAS}}$ [Eq. (14)]. Sample NC5 is the one with the lowest difference in the values of L_z, S_z, and $I^{\theta_i}_{\mathrm{XAS}}$. This is in agreement with the low magnetization and the paramagnetic character of a substantial part of the neodymium previously discussed in Sec. III D 1. Samples MNC5 and NC2 have the largest positive value for $\Delta I^{75-0}_{\mathrm{XAS}}$ and, therefore, their respective values of T_z in the direction of the plane have to be the largest.

T_z can be deduced assuming that the ratio L_z/S_z must be constant with angle. This might not be totally true because of the distortion in the charge but it is a good approximation since the spin orbit coupling energy is at least one order of magnitude higher than the exchange and the crystal field interactions estimated in Sec. III D 1. Note also that, if S_z is larger than that deduced from this ratio in such a way that the variation in T_z is negligible, the intensity and the spin will not be correlated as observed since the intensity is sensitive to the charge but not to the spin. For the estimation of T_z, L_z/S_z is set to 4.75, which is the value calculated by Teramura

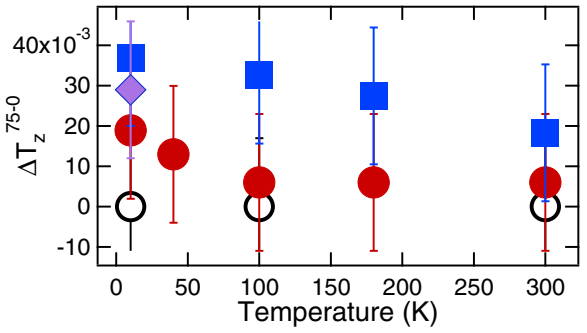

FIG. 15. Variation of ΔT_z^{75-0} with the temperature of samples NC5 (solid circles), NC10 (empty circles), MNC5 (solid squares), and NC2 (solid prism).

et al. [44]. The differences in T_z between its value at grazing incidence and normal incidence, ΔT_z^{75-0}, for each sample as a function of the temperature are shown in Fig. 15. The variations of ΔT_z^{75-0} between the samples fit very well with those predicted using only the observed variation in $\Delta I_{\mathrm{XAS}}^{75-0}$ for each sample. ΔT_z^{75-0} decreases with the temperature in a relatively different way in samples MNC5 and NC5 due to the different temperature dependence of their neodymium magnetic moments (see Fig. 11).

If a proportionality is assumed between T_z and S_z[21], then the ratio T_z/S_z yields a value that is independent of the thermal variation of the neodymium magnetic moment, i.e., it depends only on the atomic environment. Then, the difference of this ratio between the two orientations should give a measure of the asymmetry of the averaged atomic neodymium environment at each temperature. Figure 16 represents the variation of this ratio with the temperature for each sample. The largest variation occurs in sample MNC5 and the lowest in sample NC10. They are relatively large, up to 22% in sample MNC5 at RT. In this sample, the crystal field asymmetry clearly increases with the temperature indicating structural changes in the alloy which are thermally induced. EXAFS spectroscopy already detected a relatively large anisotropic anomalous thermal expansion of the cobalt subnetwork in a similar sample [17]. These structural changes are probably linked to the strains induced in the alloy during film growth and their release with the temperature, possibly favored by their interplay

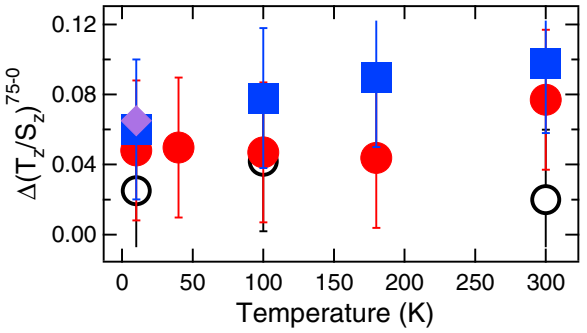

FIG. 16. Variation of $\Delta(T_z/S_z)^{75-0}$ with the temperature of samples NC5 (solid circles), NC10 (empty circles), MNC5 (solid squares), and NC2 (solid prism).

with the magnetoelastic properties of each of the magnetic environments. The importance of anelastic strains in the development of the magnetic anisotropy of these alloys is well known [11,68,69]. In fact, we have observed an irreversible reduction of about 20% in the magnetic anisotropy of our films with annealing temperatures of only 400 K [41]. The release of film strain at low temperature might be mainly driven by differences in the thermal and magnetoelastic expansion coefficients of the neodymium and cobalt subnetworks, which might explain the changes observed in Fig. 16.

The proposed deformation in the charge has to be due to the competition between the crystal field and the neodymium-cobalt indirect exchange interactions, which have to be strong enough to cause a significant rearrangement of the electronic energy levels of the $4f$ band with respect to the isolated atomic state. Such a rearrangement should be noticed in the shape of the spectra which should change with the orientation. Figures 17 and 18 show the $\Delta I_{\mathrm{XAS}}^{75-0}$ spectra of all the analyzed samples at 10 K centered at the Nd M_5 and Nd M_4 resonances, respectively. There is a clear change in the shape in all of them. The changes do not follow the shape of the I_{XAS} spectra. Therefore they are intrinsic to the spectra and they can not be totally caused by the value for the secondary electron escape length λ_e (see the Appendix). For instance, the $\Delta I_{\mathrm{XAS}}^{75-0}$ spectra of samples MNC5 and NC2 are obtained using two different λ_e values, 25 and 20 Å for MNC5 and 20 and 17 Å for sample NC2. The spectrum with the larger value of λ_e is the one drawn with a thicker line. It shows a relative change in the shape but not its suppression. There seem to be similarities in the $\Delta I_{\mathrm{XAS}}^{75-0}$ spectral shape between samples NC5 and NC10, which are the samples with the largest concentration of segregated neodymium, and between samples NC and MNC5.

The most striking change in the shape occurs in sample NC. The magnetization of neodymium in this sample at RT is very small, about ten times smaller than that measured at 10 K and it should come from a paramagnetic phase, i.e., nearly uncoupled to cobalt by indirect exchange as is deduced from its hysteresis loops in Fig. 3. However, the decrease in the ratio L_z/S_z between normal and grazing incidence is, within the error, comparable to that observed in sample MNC5. This difference decreases to nearly 0 at 10 K, when it becomes more coupled to cobalt, changing the spectrum. Figure 19 shows these changes in the $\Delta I_{\mathrm{XAS}}^{75-0}$ spectra. The fact that the $\Delta I_{\mathrm{XAS}}^{75-0}$ spectrum of sample NC at RT is not flat is a clear indicator that they have to be due to distortions in the charge caused by the crystal field. This anisotropy in the charge distribution of the $4f$ is, for instance, the cause of the anisotropic susceptibility observed in RE-hexagonal manganites [70]. The changes in $\Delta I_{\mathrm{XAS}}^{75-0}$ at 10 K with respect to the one observed at RT demonstrates that the Nd $4f$ charge is also modified by the exchange interaction with cobalt.

From these results it is deduced that the magnetic anisotropy of the neodymium subnetwork has its origin in the local crystal field whose symmetry axis is directed statistically more out of the plane than in the plane. The structural anisotropy of the cobalt sublattice, in correspondence with previous EXAFS observation, agrees with the models that explain the anisotropy in RE-TM alloys derived from a preferential arrangement of neodymium and cobalt atoms in a stratified manner as in the structure of NdFeB [71]. However, despite the

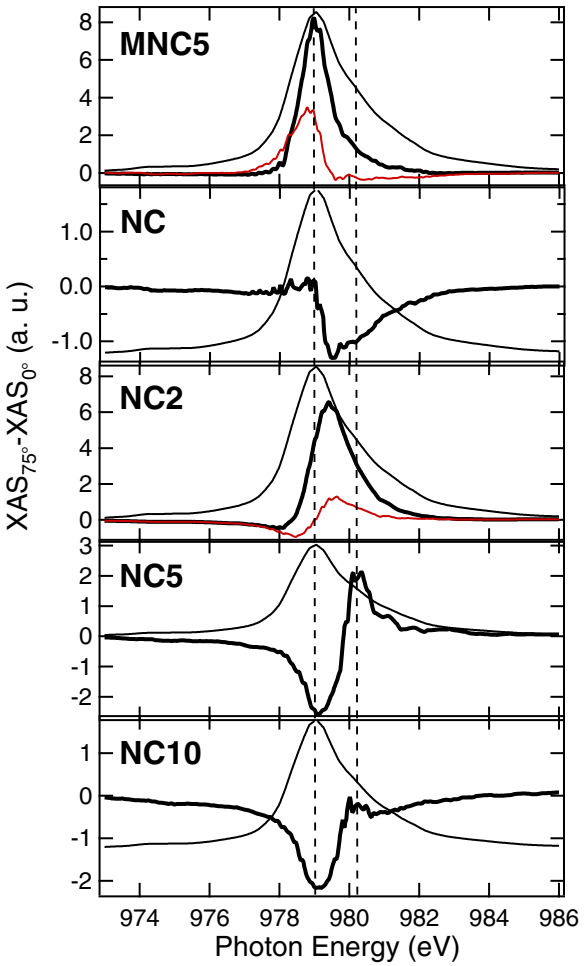

FIG. 17. $\Delta I_{\mathrm{XAS}}^{75-0}$ spectra centered at the Nd M_5 resonance of all the samples (thick line). They are compared with their Nd M_5 spectra (thin line). The red thin lines in MN5 and NC2 are the $\Delta I_{\mathrm{XAS}}^{75-0}$ spectra using a λ_e smaller than the one used in the thick line spectra.

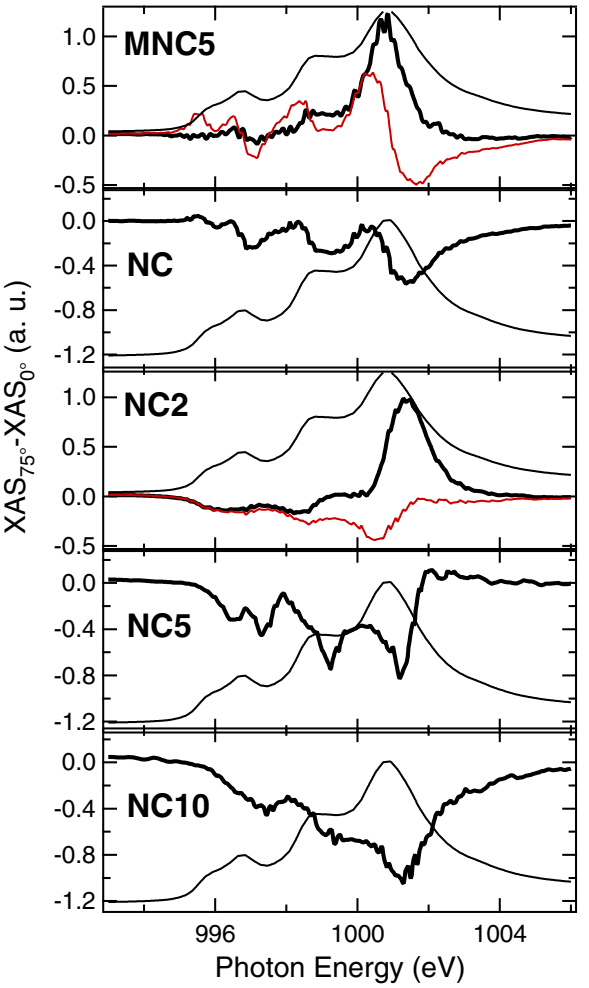

FIG. 18. $\Delta I_{\mathrm{XAS}}^{75-0}$ spectra centered at the Nd M_4 resonance of all the samples (thick line). They are compared with their Nd M_4 spectra (thin line). The red thin line in MN5 and NC2 are the $\Delta I_{\mathrm{XAS}}^{75-0}$ spectra using a λ_e smaller than the one used in the thick line spectra.

perpendicular anisotropy of neodymium in all the samples, the magnetic anisotropy of their respective alloys is only clearly perpendicular in sample MNC5. This is due to the competition with the in-plane anisotropy of Co, as in sample NC2, and/or the lack of enough magnetic coupling between neodymiun and cobalt as occurs in samples NC5 and NC10.

We find that the competition between the anisotropies of the cobalt and neodymium subnetworks is an important element to the understanding of the PMA in these alloys. This aspect has not been studied properly before because of the difficulties to analyze separately the magnetic behavior of the RE and TM subnetworks. It is possible to do it now thanks to XMCD. Sample NC2 is an interesting example of such a competition where the magnetic anisotropy of the cobalt subnetwork wins. As already discussed at the end of Sec. III C 2, the in-plane magnetic anisotropy energy of the cobalt subnetwork should be higher and/or more effective than in the rest of the samples since it is higher than the shape anisotropy and it must overcome the PMA of its neodymium subnetwork, whose energy should be of the same magnitude as in sample MNC5. This higher in-plane anisotropy energy of cobalt should be a consequence of the more efficient intermixing between neodymium and cobalt in NC2, which was expected since its concentration is closer to the eutectic points of the alloy than in samples NC5, NC10, and MNC5. Experimental evidence of the better cobalt-neodymium intermixing in this sample

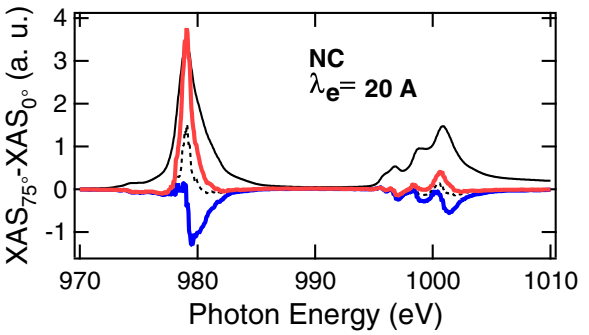

FIG. 19. $\Delta I_{\mathrm{XAS}}^{75-0}$ spectra of sample NC taken at RT (red) and 10 K (blue) using a λ_e of 20 Å. The dotted line is the $\Delta I_{\mathrm{XAS}}^{75-0}$ spectrum of the same sample taken at RT but changing λ_e to 17 Å. The black line is its Nd $M_{4,5}$ XAS spectrum rescaled 1:50.

are its bond coordination to cobalt, which is the highest of all the analyzed films (see Sec. III C 1) and the values of its neodymium and cobalt magnetic moments, which are closer to the measured in $NdCo_2$ laves [72]: 2.6 $\mu_B$for Nd (2.7 μ_B measured) and 0.8 μ_B for cobalt (1.1 μ_B measured). The good intermixing between both metals and the higher concentration of neodymium result in a magnetic coupling between both subnetworks where their magnetic moments and magnetic anisotropies should be more interrelated than in sample MNC5: sample NC2 has the largest L_z/S_z ratio for cobalt of all the samples, 0.16, which means a higher localization of the cobalt moment compared to the samples with lower neodymium concentrations; its neodymium L_z/S_z ratio is the lowest of all the samples, i.e., its $4f$ orbital is more distorted in the perpendicular direction than in the rest of samples, indicating the perturbing effect of the in-plane cobalt anisotropy.

IV. CONCLUSIONS

In summary, the origin of PMA in Nd_xCo_{1-x} amorphous alloys has been investigated by measuring the magnetic orbital and spin moments of the $3d$ cobalt and $4f$ neodymium electrons using XMCD spectroscopy at the Co $L_{2,3}$ and Nd $M_{4,5}$ edges. There is an inverse proportionality between the magnetic moment of cobalt and the magnetic moment of neodymium, as expected. However, this relationship was not found to be correlated with the relative concentration of neodymium and cobalt in the samples evidencing segregation in the alloys. Analysis of the temperature dependence of the neodymium magnetic moment using the random anisotropy model confirms a segregation, indicating a speromagnetic Nd-rich phase at values ranging from 40% to 75% atomic concentrations. The segregation and formation of inhomogeneities in the films is coherent with that expected from the Nd-Co phase diagram, indicating that the sputtering deposition process made at RT does not set the alloy system completely out of equilibrium. The particular conditions in which cobalt and neodymium segregates in the alloys with low neodymium concentration causes a significant enhancement of the cobalt spin and orbital moments, reaching values as high as 1.95 μ_B and 0.25 μ_B, respectively. The anisotropy of the orbital moment of cobalt is in the film plane in all of the samples in agreement with a structural anisotropy for the cobalt subnetwork previously observed by EXAFS. On the other hand, the magnetic moment of the neodymium atoms is always larger in the perpendicular direction. This is a direct experimental confirmation of the single ion model applied to these alloys, according to which the average magnetic anisotropy of the RE ions is perpendicular, being responsible of the PMA of the alloys, with the important addition that the TM anisotropy is in the plane. We found that the competition between the anisotropies of both subnetworks is more effective for cobalt when the concentration of neodymium is closer to the eutectic point of the alloy, explaining why the PMA in these alloys vanishes in this range of concentrations. Our experiment demonstrates that the $4f$ electrons in neodymium atoms are more influenced by interatomic interactions than what it is commonly assumed. The ratio L_z/S_z of their $4f$ orbitals changes with the sample orientation angle with respect to the magnetic field, being higher and closer to the atomic value expected at normal orientation and smaller at grazing angles. This finding is well understood under the assumption that the Nd $4f$ orbital is more distorted in the hard magnetic axis by the effect of an anisotropic crystal field. The magnetic anisotropy energy should be proportional to this distortion, which we demonstrate is accessible by applying the XMCD sum rules for the spin and intensity at the Nd $M_{4,5}$ resonances. If the needed models would be developed, the atomic scale study performed here would allow to address and quantify the macroscopic anisotropy of each subnetwork and the relation to their magnetic interaction. This work is expected to be of interest not only for the understanding of the magnetic anisotropy in amorphous magnetic thin films but for RE-TM alloys and compounds in general, and it hopefully motivates further studies and theoretical developments.

ACKNOWLEDGMENTS

Work supported by Ministerio de Economía y Competitividad (Gobierno de España) (Spain) grants #FIS2013-45469 and FIS2016-76058. R. Cid acknowledges support from Spanish Ministerio de Educación y Cultura (MEC) (Gobierno de España) under FPU grant. M.Valvidares acknowledges a MEC (Gobierno de España) grant for Specialization in International Organizations, ES-2004-0153.

APPENDIX: ANALYSIS PROCEDURE OF XMCD SPECTRA. SATURATION EFFECTS CORRECTION

The spectra obtained using TEY are distorted due to saturation of the emitted electron intensity. This distortion depends on the ratio between the mean depths from where secondary electrons are detected (λ_e) and the x-ray photons are absorbed [$\lambda_x(E) = \cos\theta_i/\mu^{\theta_i}(E)$], where θ_i is the angle of incidence with respect to the normal to the surface and $\mu^{\theta_i}(E)$ is the absorption coefficient for that specific incident angle. The smaller this ratio λ_e/λ_x is the smaller is the saturation effect. The effect becomes stronger at larger incidence angles θ_i (grazing incidence) because of the proportionality of λ_x with the cosine of θ_i. The relation between the TEY detected and normalized to the incident beam $I^{\theta_i}_{\rm exp}$ and the absorption coefficient $\mu^{\theta_i}(E)$ is [73]

$$\frac{I^{\theta_i}_{\rm exp}(E)}{A^{\theta_i}_0} = \frac{\mu^{\theta_i}(E)}{\left(1+\frac{\lambda_e}{\lambda_x(E)}\right)} + I^{\theta_i}_B(E), \tag{A1}$$

where it has been assumed that the thickness of the film ($\approx$300 Å) is much higher than λ_e ($\leqslant$35 Å). $A^{\theta_i}_0$ is a constant and $I^{\theta_i}_B(E)$ is a background that varies smoothly with photon energy. Both factors depend on the details of the experiment. We define the experimental absorption coefficient obtained at the incidence angle θ_i, $\mu^{\theta_i}_{\rm exp}(E)$, as $\mu^{\theta_i}_{\rm exp}(E) = \frac{I_{\rm exp}(E)}{A^{\theta_i}_0} - I^{\theta_i}_B(E)$.

Therefore, to determine the true absorption coefficient $\mu^{\theta_i}(E)$, starting from the TEY spectrum $I^{\theta_i}_{\rm exp}(E)$, it is required to know with accuracy the specific value of λ_e and all the experimental factors involved in the experiment [constant $A^{\theta_i}_0$ and background $I^{\theta_i}_B(E)$], something that is not always possible in a regular x-ray absorption experiment. The approach used by us is to take as a reference the tabulated absorption coefficient

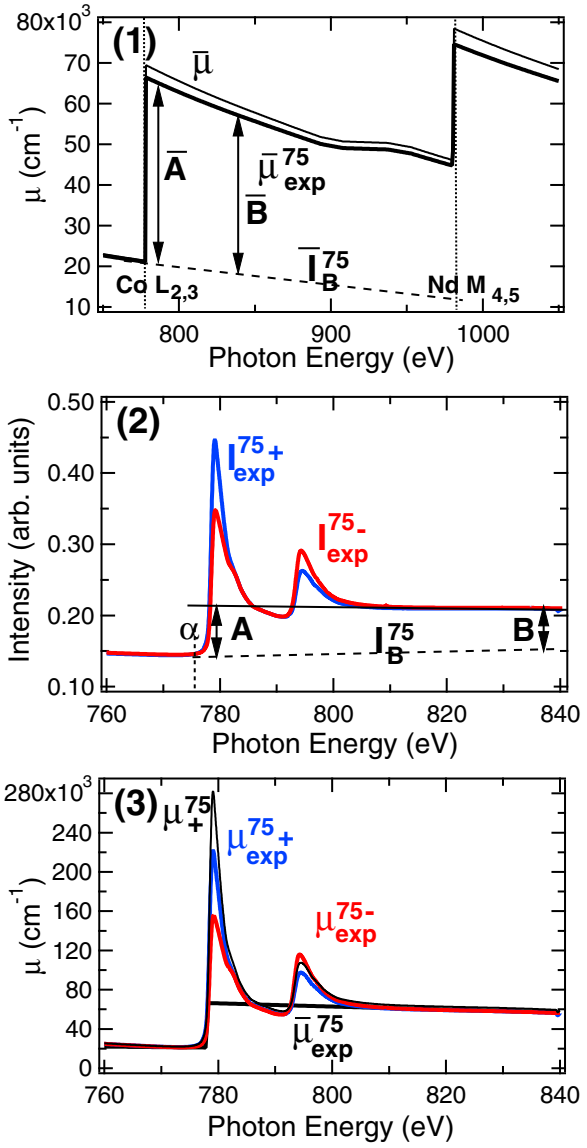

FIG. 20. Process to create $\mu^{75}_{\rm exp}(E)$, an experimental absorption coefficient (saturation effects uncorrected), starting from the experimental absorbed intensity spectra at the angle of incidence $\theta_i = 75°$, $I^{75+,-}_{\rm exp}(E)$, and the tabulated absorption coefficient of the alloy, $\bar{\mu}(E)$. (1) shows the saturated absorption coefficient, $\bar{\mu}^{75}_{\rm exp}(E)$, for the Co $L_{2,3}$ and Nd $M_{4,5}$ absorption edges obtained introducing $\bar{\mu}(E)$ in equation (A1) in substitution of $\mu^{\theta_i}(E)$. The dashed line is $\bar{I}^{75}_B(E)$, the background for the Co $L_{2,3}$ edge. (2) shows the way to eliminate the linear background $I^{75}_B(E)$ in the experimental $I^{75+,-}_{\rm exp}(E)$ spectra. $I^{75}_B(E)$ is the same for both polarizations. The ratio A_{75}/B_{75} must be the same that the obtained in $\mu^{75}_{\rm exp}(E)$, $\bar{A}_{75}/\bar{B}_{75}$ (1). α is the point where the intensity is taken to be zero. (3) is the final result after subtracting $I^{75}_B(E)$ to $I^{75+,-}_{\rm exp}(E)$, multiplying it by $\bar{A}_{75}$ and adding the linear background $\bar{I}^{75}_B(E)$.

of the nonresonant part of the spectra [74], $\bar{\mu}(E)$, and to try different values of λ_e close to the expected value according to the concentrations of the analyzed alloys [23,73,75,76]. The chosen values for λ_e ranged from 33 Å in NC10 to 19 Å in NC.

The expected experimental nonresonant absorption coefficient at an incidence angle θ_i, $\bar{\mu}^{\theta_i}_{\rm exp}(E)$, can be obtained substituting $\mu^{\theta_i}(E)$ by $\bar{\mu}(E)$ in Eq. (A1). The experimental TEY spectrum $I^{\theta_i}_{\rm exp}$ should scale with $\bar{\mu}^{\theta_i}_{\rm exp}(E)$ once the background $I^{\theta_i}_B(E)$ is removed. This background is usually assumed to be linear with the photon energy E. Then, the conversion of the TEY spectrum, $I^{\theta_i}_{\rm exp}$, to the absorption coefficient not corrected from saturation, $\mu^{\theta_i}_{\rm exp}(E)$, is done in three steps (see Fig. 20). In the first step, a linear background is removed from the TEY spectrum $I^{\theta_i}_{\rm exp}(E)$ in such a way that the start of the absorption edge is set to zero intensity and the intensity of the spectrum at its highest photon energy, far away from the resonance region, keeps the same ratio in intensity as the intensity at the step of the absorption edge in the nonresonant spectrum $\bar{\mu}^{\theta_i}_{\rm exp}(E)$. In the second step, the spectrum is multiplied by a constant to get the same change in intensity in absorption coefficient units ($\rm cm^{-1}$) at the absorption edge as in $\bar{\mu}^{\theta_i}_{\rm exp}(E)$. The final step is to add a linear background caused by absorption edges at lower photon energies. This background is the same as the expected experimental nonresonant spectrum $\bar{\mu}^{\theta_i}(E)$. The final result is shown in Fig. 20 where $I^{\theta_i}_{\rm exp}(E)$, $\bar{\mu}(E)$, $\bar{\mu}^{\theta_i}_{\rm exp}(E)$, and $\mu^{\theta_i}_{\rm exp}(E)$ are compared at $\theta_i = 75°$. The "true" absorption coefficient at a θ_i incidence angle with the saturation effects corrected, $\mu^{\theta_i}(E)$, is obtained introducing $\mu^{\theta_i}_{\rm exp}(E)$ in Eq. (A1). The XMCD spectrum at each orientation θ_i, $I^{\theta_i}_{\rm XMCD}(E)$, is defined as

$$I^{\theta_i}_{\rm XMCD}(E) = \mu^{\theta_i}_{+}(E) - \mu^{\theta_i}_{-}(E), \qquad \text{(A2)}$$

where $\mu^{\theta_i}_{+}(E)$ and $\mu^{\theta_i}_{-}(E)$ are the absorption coefficient using right- and left-hand circular polarizations, respectively.

We stress here the importance of checking if the acquired spectra are identical in the nonresonant region of the spectra, i.e., in the regions not affected by magnetism (pre-edge and post-edge regions) when the spectra are obtained at the same incidence angle but with inverse circular polarization or reversed magnetic field before the described process to extract the related absorption coefficients is started. Otherwise, spectra might be contaminated from an external source and the spin and orbital moments derived from their analysis might be unreliable.

The absorption coefficients $\mu^{\theta_i}(E)$ of the same sample obtained at the same temperature should be identical at any incidence angle θ_i, at least, in the pre-edge and post-edge regions. The coincidence of these regions found in our spectra was very good, of the order of 1‰, obtaining similar slopes at the pre-edge and post-edge regions.

[1] P. Chaudhari, J. Cuomo, and R. Gambino, Appl. Phys. Lett. **22**, 337 (1973).

[2] R. L. Stamps, S. Breitkreutz, J. Akerman, A. V. Chumak, Y. Otani, G. E. Bauer, J. U. Thiele, M. Bowen, S. A. Majetich, M. Klüi *et al.*, J. Phys. D: Appl. Phys. **47**, 333001 (2014).

[3] S. Alebrand, M. Gottwald, M. Hehn, D. Steil, M. Cinchetti, D. Lacour, E. E. Fullerton, M. Aeschlimann, and S. Mangin, Appl. Phys. Lett. **101**, 162408 (2012).

[4] K. Chen, D. Lott, F. Radu, F. Choueikani, E. Otero, and P. Ohresser, Sci. Rep. **5**, 18377 (2015).

[5] C. Blanco-Roldán, C. Quirós, A. Sorrentino, A. Hierro-Rodríguez, L. M. Álvarez-Prado, R. Valcárcel, M. Duch, N. Torras, J. Esteve, J. I. Martín *et al.*, Nat. Commun. **6**, 8196 (2015).

[6] A. Hierro-Rodriguez, R. Cid, M. Vélez, G. Rodriguez-Rodriguez, J. I. Martín, L. M. Álvarez-Prado, and J. M. Alameda, Phys. Rev. Lett. **109**, 117202 (2012).

[7] A. Hierro-Rodriguez, M. Vélez, R. Morales, N. Soriano, G. Rodríguez-Rodríguez, L. M. Álvarez-Prado, J. I. Martín, and J. M. Alameda, Phys. Rev. B **88**, 174411 (2013).

[8] N. Akulov, Z. Phys. **100**, 197 (1936).

[9] H. B. Callen and E. Callen, J. Phys. Chem. Solids **27**, 1271 (1966).

[10] R. Skomski and D. J. Sellmeyer, J. Rare Earths **27**, 675 (2009).

[11] X. Yan, M. Hirscher, T. Egami, and E. E. Marinero, Phys. Rev. B **43**, 9300 (1991).

[12] V. G. Harris and T. Pokhil, Phys. Rev. Lett. **87**, 067207 (2001).

[13] Y. Nishihara, T. Katayama, Y. Yamaguchi, S. Ogawa, and T. Tsushima, Jpn. J. Appl. Phys. **17**, 1083 (1978).

[14] F. Hellman and E. M. Gyorgy, Phys. Rev. Lett. **68**, 1391 (1992).

[15] D. Mergel, H. Heitmann, and P. Hansen, Phys. Rev. B **47**, 882 (1993).

[16] G. Miletic and Z. Blazina, J. Magn. Magn. Mater. **321**, 3888 (2009).

[17] J. Díaz, R. Cid, A. Hierro, L. M. Álvarez-Prado, C. Quirós, and J. M. Alameda, J. Phys.: Condens. Matter **25**, 426002 (2013).

[18] B. T. Thole, G. van der Laan, and G. A. Sawatzky, Phys. Rev. Lett. **55**, 2086 (1985).

[19] B. T. Thole, P. Carra, F. Sette, and G. van der Laan, Phys. Rev. Lett. **68**, 1943 (1992).

[20] M. Altarelli, Phys. Rev. B **47**, 597 (1993).

[21] P. Carra, B. T. Thole, M. Altarelli, and X. Wang, Phys. Rev. Lett. **70**, 694 (1993).

[22] J. B. Goedkoop, B. T. Thole, G. van der Laan, G. A. Sawatzky, F. M. F. de Groot, and J. C. Fuggle, Phys. Rev. B **37**, 2086 (1988).

[23] J. Vogel, M. Sacchi, R. J. Kappert, J. C. Fuggle, J. B. Goedkoop, N. B. Brookes, G. van der Laan, and E. E. Marinero, J. Magn. Magn. Mater. **150**, 293 (1995).

[24] S. P. Collins, D. Laundy, C. C. Tang, and G. van der Laan, J. Phys.: Condens. Matter **7**, 9325 (1995).

[25] K. Chen, D. Lott, F. Radu, F. Choueikani, E. Otero, and P. Ohresser, Phys. Rev. B **91**, 024409 (2015).

[26] T. Okane, Y. Takeda, H. Yamagami, A. Fujimori, Y. Matsumoto, N. Kimura, T. Komatsubara, and H. Aoki, Phys. Rev. B **86**, 125138 (2012).

[27] V. Cuartero, S. Lafuerza, G. Subías, J. García, E. Schierle, J. Blasco, and J. Herrero-Albillos, Phys. Rev. B **91**, 165111 (2015).

[28] G. van der Laan, E. Arenholz, A. Schmehl, and D. G. Schlom, Phys. Rev. Lett. **100**, 067403 (2008).

[29] J. Stöhr, J. Magn. Magn. Mater. **200**, 470 (1999).

[30] C. Andersson, B. Sanyal, O. Eriksson, L. Nordström, O. Karis, D. Arvanitis, T. Konishi, E. Holub-Krappe, and J. H. Dunn, Phys. Rev. Lett. **99**, 177207 (2007).

[31] R. Skomski, A. Kashyap, and A. Enders, J. Appl. Phys. **109**, 07E143 (2011).

[32] K. Baberschke, in *Band-Ferromagnetism: Ground-State and Finite-Temperature Phenomena* (Springer, Berlin, Heidelberg, 2001), Chap. Anisotropy in Magnetism, pp. 27–45.

[33] S. Pascarelli, M. P. Ruffoni, A. Trapananti, O. Mathon, C. Detlefs, M. Pasquale, A. Magni, C. P. Sasso, F. Celegato, E. Olivetti *et al.*, Phys. Rev. B **81**, 020406 (2010).

[34] P. Bruno, Phys. Rev. B **39**, 865 (1989).

[35] D. Weller, J. Stöhr, R. Nakajima, A. Carl, M. G. Samant, C. Chappert, R. Mégy, P. Beauvillain, P. Veillet, and G. A. Held, Phys. Rev. Lett. **75**, 3752 (1995).

[36] K. H. J. Buschow, Rep. Prog. Phys. **40**, 1179 (1977).

[37] A. Miedema, P. de Chatel, and F. de Boer, Physica B+C **100**, 1 (1980).

[38] J. Díaz, R. Morales, S. M. Valvidares, and J. M. Alameda, Phys. Rev. B **72**, 144413 (2005).

[39] M. Vélez, C. Mény, S. M. Valvidares, J. Diaz, R. Morales, L. M. Alvarez-Prado, P. Panissod, and J. M. Alameda, Eur. Phys. J. B **41**, 517 (2004).

[40] B. Predel, in *Co-Nd (Cobalt-Neodymium)* (Springer, Berlin, Heidelberg, 1993), pp. 1–3.

[41] R. Cid, G. Rodríguez-Rodríguez, L. Álvarez-Prado, J. Díaz, and J. Alameda, J. Magn. Magn. Mater. **316**, e446 (2007)

[42] See Supplemental Material at http://link.aps.org/supplemental/10.1103/PhysRevB.95.224402 for compilation of XMCD spectra used in the analysis.

[43] J. Stöhr and H. König, Phys. Rev. Lett. **75**, 3748 (1995).

[44] Y. Teramura, A. Tanaka, B. Thole, and T. Jo, J. Phys. Soc. Jpn. **65**, 3056 (1996).

[45] J. Stöhr and H. C. Siegmann, in *Magnetism: From Fundamentals to Nanoscale Dynamics*, Springer Series Solid-State Science (Springer-Verlag, Berlin, Heidelberg, 2006), Vol. 152, p. 401.

[46] M. Hehn, S. Padovani, K. Ounadjela, and J. P. Bucher, Phys. Rev. B **54**, 3428 (1996).

[47] A. Hubert and R. Schäfer, in *Magnetic Domains* (Springer, Berlin, Heidelberg, 1998), pp. 27–45.

[48] L. M. Alvarez-Prado, G. T. Pérez, R. Morales, F. H. Salas, and J. M. Alameda, Phys. Rev. B **56**, 3306 (1997).

[49] R. Cid, J. Díaz, L. M. Álvarez-Prado, J. M. Alameda, S. M. Valvidares, J. C. Cezar, and N. B. Brookes, J. Phys.: Conf. Ser. **200**, 072017 (2010).

[50] J. M. Alameda, D. Givord, R. Lemaire, Q. Lu, S. B. Palmer, and F. Tasset, J. Phys. Colloq. **43**, 133 (1982).

[51] R. Cochrane, R. Harris, and M. Zuckermann, Phys. Rep. **48**, 1 (1978).

[52] R. Alben, J. J. Becker, and M. C. Chi, J. of Appl. Phys. **49**, 1653 (1978).

[53] J. F. Elliott, S. Legvold, and F. H. Spedding, Phys. Rev. **94**, 50 (1954).

[54] S. K. Malik, F. J. Arlinghaus, and W. E. Wallace, Phys. Rev. B **16**, 1242 (1977).

[55] T. W. Capehart, J. F. Herbst, R. K. Mishra, and F. E. Pinkerton, Phys. Rev. B **52**, 7907 (1995).

[56] K. Buschow, M. Brouha, J. Biesterbos, and A. Dirks, Physica B+C **91**, 261 (1977).

[57] F. Rei-Yi, D. Dao-sheng, L. Zun-xiao, W. Hong, and J. Yu-ping, J. Magn. Magn. Mater. **58**, 273 (1986).

[58] T. Koide, H. Miyauchi, J. Okamoto, T. Shidara, A. Fujimori, H. Fukutani, K. Amemiya, H. Takeshita, S. Yuasa, T. Katayama *et al.*, Phys. Rev. Lett. **87**, 257201 (2001).

[59] G. Apai, J. F. Hamilton, J. Stöhr, and A. Thompson, Phys. Rev. Lett. **43**, 165 (1979).

[60] O. Mironets, H. L. Meyerheim, C. Tusche, V. S. Stepanyuk, E. Soyka, H. Hong, P. Zschack, N. Jeutter, R. Felici, and J. Kirschner, Phys. Rev. B **79**, 035406 (2009).
[61] D. J. Keavney, E. E. Fullerton, D. Li, C. H. Sowers, S. D. Bader, K. Goodman, J. G. Tobin, and R. Carr, Phys. Rev. B **57**, 5291 (1998).
[62] I. V. Solovyev, P. H. Dederichs, and I. Mertig, Phys. Rev. B **52**, 13419 (1995).
[63] R. Harris, M. Plischke, and M. J. Zuckermann, Phys. Rev. Lett. **31**, 160 (1973).
[64] R. Harris and D. Zobin, J. Phys. F **7**, 337 (1977).
[65] J. M. D. Coey, Can. J. Phys. **65**, 1210 (1987).
[66] I. A. Campbell, J. Phys. F **2**, L47 (1972).
[67] G. Y. Guo, H. Ebert, W. M. Temmerman, and P. J. Durham, Phys. Rev. B **50**, 3861 (1994).
[68] V. G. Harris, K. D. Aylesworth, B. N. Das, W. T. Elam, and N. C. Koon, Phys. Rev. Lett. **69**, 1939 (1992).
[69] M. Ohta, K. Yamada, Y. Satake, A. Fujita, and K. Fukamichi, Mater. Trans. **44**, 2605 (2003).
[70] V. Skumryev, M. D. Kuz'min, M. Gospodinov, and J. Fontcuberta, Phys. Rev. B **79**, 212414 (2009).
[71] M.-F. Rossignol and J.-P. Yonnet, in *Magnetism: Materials and Applications*, edited by É. du Trémolet de Lacheisserie, D. Gignoux, and M. Schlenker, Grenoble Science Series (Springer, New York, 2005), Vol. I and II, p. 56.
[72] W. Wallace, in *Rare Earth Intermetallics*, edited by W. Wallace (Academic Press, London, 1973), p. 145.
[73] R. Nakajima, J. Stöhr, and Y. U. Idzerda, Phys. Rev. B **59**, 6421 (1999).
[74] E. G. B. L. Henke and J. Davis, At. Data Nucl. Data Tables **54**, 181 (1993).
[75] J. Vogel and M. Sacchi, J. Electron Spectrosc. Relat. Phenom. **67**, 181 (1994).
[76] B. H. Frazer, B. Gilbert, B. R. Sonderegger, and G. D. Stasio, Surf. Sci. **537**, 161 (2003).